

(12)

THE MAGNETIC EFFECTS OF SHALLOW WATER INTERNAL SOLITONS

Alan D. Chave

AD-A165 852

SIO REFERENCE SERIES

Prepared for the Office of Naval Research under  
Contract N00014-85-C-0104

March 1986

SIO Reference 86-7

DTIC  
ELECTE  
MAR 28 1986  
S B

DISTRIBUTION STATEMENT A

Approved for public release  
Distribution Unlimited

University of California

Scripps Institution of Oceanography

DTIC FILE COPY

86 3 23 005

REPORT DOCUMENTATION PAGE		READ INSTRUCTIONS BEFORE COMPLETING FORM
1. REPORT NUMBER	2. GOVT ACCESSION NO.	3. RECIPIENT'S CATALOG NUMBER
4. TITLE (and Subtitle) The Magnetic Effects of Shallow Water Internal Solitons		5. TYPE OF REPORT & PERIOD COVERED
7. AUTHOR(s) Alan D. Chave		6. PERFORMING ORG. REPORT NUMBER SIO Reference 86-7
9. PERFORMING ORGANIZATION NAME AND ADDRESS Institute of Geophysics & Planetary Physics Scripps Institution of Oceanography University of California, San Diego, La Jolla, CA		8. CONTRACT OR GRANT NUMBER(s) ONR N00014-85-C-0104
11. CONTROLLING OFFICE NAME AND ADDRESS Office of Naval Research Arlington, VA 22217		10. PROGRAM ELEMENT, PROJECT, TASK AREA & WORK UNIT NUMBERS
14. MONITORING AGENCY NAME & ADDRESS (if different from Controlling Office)		12. REPORT DATE March 1986
		13. NUMBER OF PAGES 48
		15. SECURITY CLASS. (of this report) .
		15a. DECLASSIFICATION/DOWNGRADING SCHEDULE
16. DISTRIBUTION STATEMENT (of this Report)  Approved for public release; distribution unlimited		
17. DISTRIBUTION STATEMENT (of the abstract entered in Block 20, if different from Report)		
18. SUPPLEMENTARY NOTES		
19. KEY WORDS (Continue on reverse side if necessary and identify by block number)		
20. ABSTRACT (Continue on reverse side if necessary and identify by block number)  see attached sheet		

## Introduction

Internal waves are a ubiquitous feature of the deep ocean, occurring on spatial scales from meters to kilometers and time scales from minutes to a day. A unified picture of oceanic internal waves was given by the kinematic spectral description of Garrett and Munk [1972, 1979]. This model combined linear theory and experimental data to yield predictions of displacement and velocity spectra and the associated coherence functions for both moored and towed sensors. Since they are best described as a stochastic phenomenon with a wideband frequency-wavenumber spectrum, statements about their instantaneous amplitudes or velocities have little meaning.

By contrast, internal waves are sometimes observed on the continental shelves or in enclosed, marginal seas as quasi-deterministic groups of coherent waves with well-defined periods and wavelengths. These wave packets generally propagate toward land from a localized source region, and are believed to originate by the interaction of the ocean tides with abrupt changes in bathymetry. The waves have periods of minutes to an hour and wavelengths ranging from 50 m to a few km, and the associated internal displacements range from 5 to as much as 100 m. The surface signatures of these internal waves are frequently observed in either optical or radar imagery from aircraft or earth orbiting satellites.

Since internal waves are a common feature of the oceans, there has been some interest in computing their electromagnetic effects in order to assess their role in the oceanic electromagnetic environment. Deep ocean internal waves have been studied by Beal and Weaver [1970] and Podney [1975] using simple, two-layer or constant buoyancy frequency models. Petersen and Poehls [1982] and Chave [1984] produced more realistic spectral descriptions by combining the Garrett-Munk description of the internal wave field with an appropriate form of the Maxwell equations of electromagnetism. The results indicate that the spectral levels are fairly high in the ocean's interior, but boundary effects reduce the spectra by decades at the seafloor and sea surface. Internal wave-induced magnetic fields may also serve as a significant noise source in aeromagnetic applications.

This report extends the analysis to cover the electromagnetic effects of coastal internal wave packets. While no observations of the electromagnetic fields produced by them have been reported, the large amplitude of shallow water internal waves is expected to induce substantial electromagnetic anomalies. The report is organized into five sections. The next part contains a review of oceanographic observations of internal wave packets from both surface ships and satellite imagery. Section 3 outlines the hydrodynamic theory for nonlinear internal waves. Section 4 contains a derivation of expressions for the electromagnetic fields produced by an isolated internal soliton both at the seafloor and above the sea surface. The last part of the report contains a discussion of the theoretical results, including a detailed look at the predicted magnetic fields using measured parameters from three well-documented occurrences of internal wave packets.

Scripps Institution of Oceanography  
University of California at San Diego

The Magnetic Effects of Shallow Water Internal Solitons

Alan D. Chave

Institute of Geophysics and Planetary Physics  
Scripps Institution of Oceanography  
La Jolla, CA 92093

Prepared for the Office of Naval Research under  
Contract N00014-85-C-0104

March 1986

SIO Reference 86-7

DTIC  
ELECTE  
MAR 28 1986  
S B

## Introduction

Internal waves are a ubiquitous feature of the deep ocean, occurring on spatial scales from meters to kilometers and time scales from minutes to a day. A unified picture of oceanic internal waves was given by the kinematic spectral description of Garrett and Munk (1972, 1979). This model combined linear theory and experimental data to yield predictions of displacement and velocity spectra and the associated coherence functions for both moored and towed sensors. Since they are best described as a stochastic phenomenon with a wideband frequency-wavenumber spectrum, statements about their instantaneous amplitudes or velocities have little meaning.

By contrast, internal waves are sometimes observed on the continental shelves or in enclosed, marginal seas as quasi-deterministic groups of coherent waves with well-defined periods and wavelengths. These wave packets generally propagate toward land from a localized source region, and are believed to originate by the interaction of the ocean tides with abrupt changes in bathymetry. The waves have periods of minutes to an hour and wavelengths ranging from 50 m to a few km, and the associated internal displacements range from 5 to as much as 100 m. The surface signatures of these internal waves are frequently observed in either optical or radar imagery from aircraft or earth orbiting satellites.

Since internal waves are a common feature of the oceans, there has been some interest in computing their electromagnetic effects in order to assess their role in the oceanic electromagnetic environment. Deep ocean internal waves have been studied by Beal and Weaver (1970) and Podney (1975) using simple, two-layer or constant buoyancy frequency models. Petersen and Poehls (1982) and Chave (1984) produced more realistic spectral descriptions by combining the Garrett-Munk description of the internal wave field with an appropriate form of the Maxwell equations of electromagnetism. The results indicate that the spectral levels are fairly high in the ocean's interior, but boundary effects reduce the spectra by decades at the seafloor and sea surface. Internal wave-induced magnetic fields may also serve as a significant noise source in aeromagnetic applications.

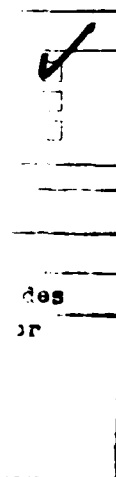
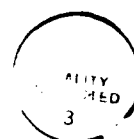
This report extends the analysis to cover the electromagnetic effects of coastal internal wave packets. While no observations of the electromagnetic fields produced by them have been reported, the large amplitude of shallow water internal waves is expected to induce substantial electromagnetic anomalies. The report is organized into five sections. The next part contains a review of oceanographic observations of internal wave packets from both surface ships and satellite imagery. Section 3 outlines the hydrodynamic theory for nonlinear internal waves. Section 4 contains a derivation of expressions for the electromagnetic fields produced by an isolated internal soliton both at the seafloor and above the sea surface. The last part of the report contains a discussion of the theoretical results, including a detailed look at the predicted magnetic fields using measured parameters from three well-documented occurrences of internal wave packets.

## Background

Narrow, linear, propagating zones of disturbed water or breaking waves in an otherwise calm sea have been reported by mariners for at least a century, especially from the island archipelagos of the western Pacific and Indian Oceans. These are undoubtedly the surface manifestations of very large-scale oceanic internal waves. The first scientific evidence connecting these surface effects with internal waves is due to Perry and Schimke (1965), who made repeated bathythermograph casts through several lines of breakers that passed the research vessel *Pioneer* in the Andaman Sea north of Sumatra. They were able to infer the existence of internal wave packets of 80 m amplitude beneath zones of surface whitecaps 200–800 m wide, spaced about 3200 m apart, and extending from horizon-to-horizon.

Subsequently, periodic or quasi-periodic features on the ocean's surface were detected in optical satellite images taken from around the world, including the east and west coasts of North America and Africa, the Gulf of California, northern South America, the central Pacific, and the Celebes Sea [Apel *et al.*, 1975a, 1976]. The internal wave origin of these lineaments was established by near-simultaneous satellite and ship-based observations in the New York Bight [Apel *et al.*, 1975b]. There are two mechanisms by which internal waves can modulate the short wavelength structure of the sea surface to produce a visible effect. The first of these is due to

1A-1



variations in surface water velocity that sweep together surface oils in zones of convergence, changing the optical reflectivity (Ewing, 1950). The second mechanism requires focussing of capillary wave energy in zones of convergence due to changes in the surface stress field, resulting in increased roughness and reduced reflectivity (Gargett and Hughes, 1972). In either instance, sub-surface wave structure causes surface changes that may be sensed remotely, assuming light wind conditions and a proper solar illumination angle.

Similar results have been achieved using synthetic aperture radar (SAR) from both aircraft (Elachi and Apel, 1976) and the Seasat satellite (Trask and Briscoe, 1983; Apel and Gonzalez, 1983; Fu and Holt, 1984). Consistency of the images with an internal wave origin have been demonstrated indirectly. SAR offers several advantages over optical imaging, including insensitivity to the presence of clouds, weather, and darkness or an improper angle of illumination.

A number of common features of the internal wave images in continental shelf regions have come out of these studies. First, the waves occur in groups or packets of typical width 3 to 5 km landward of the continental slope. The packets are separated by distances of order 15 or 30 km, corresponding to time intervals of about 12 or 24 hours, suggesting a connection with the semidiurnal or diurnal tides. Second, the wave crests are oriented parallel to the local bottom topography, and may be refracted significantly in the presence of abrupt changes in bathymetry. Third, the wavelengths within a given packet vary from 200 to 4000 m, depending on the geographical area, and there is a monotonic decrease in wavelength from front to back within the group. Fourth, the length of the wave crests ranges from a few to over 100 km, and the crests are curved with their convex sides pointing in the propagation direction. Finally, as the packet progresses onto the shelf and into shallower water, there is evidence for an increase in the wavelengths, suggesting some combination of nonlinear and dispersive effects.

The behavior of large-scale internal wave packets have been observed *in-situ* using a variety of sensors, including moored or towed thermistor chains, current meters, conductivity-temperature-depth (CTD) profilers, expendable bathythermographs (XBT), and acoustic scanners. These studies may be classified into two groups according to the water depth and wave ampli-

tude. The shallow water and continental shelf work of Halpern 1971 and Haury *et al.* 1979 in Massachusetts Bay, Ingram 1978 in the St. Lawrence estuary, Curtin and Mooers 1975 off of the Oregon coast, and Gargett 1976 near Vancouver Island is confined to water that is generally less than 100 m deep. The observations typically show short period (5–10 minutes), relatively low amplitude (5–10 m) oscillations of the thermocline in conjunction with surface rips or lineations of the type seen in satellite images. The packet group velocities range from 25 to 90 cm s<sup>-1</sup>, with the large spread undoubtedly influenced by advection from local water currents. As was inferred from satellite sensors, the wavelengths within a given group decrease from front to back, and individual elements are most easily distinguished at the front of the packet. A correlation of the occurrence of internal waves with a change in the tide, usually from ebb to flood, is noticeable, and the spacing of wave groups is also consistent with a tidal generation mechanism. For a detailed view of internal wave packet evolution in shallow water, see Haury *et al.* [1979], who used high frequency sonar to view their development in time.

The deep water studies of Sandstrom and Elliot 1984 on the outer continental shelf off Nova Scotia, Ziegenbein 1969, 1970 near the Straits of Gibraltar, Osborne and Burch 1980 in the Andaman Sea, and Apel *et al.* 1985 in the Sulu Sea show far more dramatic internal wave signatures. Sandstrom and Elliot 1984 used acoustic and CTD methods to examine internal waves with amplitudes to 60 m at the edge of the Scotian shelf. Each group contained only a few (2–4) individual elements, and were seen to break up within about 10 km of their appearance near the shelf edge, a behavior at variance with typical satellite observations. They also suggested that mixing by these tidally-produced waves was a primary mechanism to supply nutrients to the euphotic zone at the shelf-slope break, accounting for the high biological productivity of that region. Ziegenbein [1969, 1970] used moored thermistor chains in water 800 to 1000 m deep to study short internal wave packets. The groups of internal waves were associated with a longer duration internal front characterized by a depression of the thermocline by about 40 m. Oscillations of this front began about 40 minutes after its first arrival, with amplitudes of as much as 40 m peak-to-peak. The group velocities of the wave packets ranged from 1.6 to 2.2 m/s, and the



repeat time of the groups indicated a tidal association, with the strongest events separated by 24 hours.

By far the best documented occurrences of nonlinear internal wave packets are from marginal seas in Southeast Asia, where a combination of satellite images and current meter, CTD, XBT, acoustic depth sounding, and surface observations have been applied. Osborne and Burch (1980) measured packets of internal waves with a semidiurnal recurrence time that was markedly modulated by the twice monthly springtide. Amplitudes to 60 m were seen that were always in the form of depressions from a normal thermocline, and the elements of a wave group were rank-ordered, with the longest wavelengths at the front. The ocean stratification could be roughly fit by a two-layer model with an upper region of 230 m thickness underlain by an 860 m thick zone. Velocities of about 56 cm/s in the direction of packet propagation occurred in the top layer, while a velocity of about 15 cm/s with the opposite direction was seen below this. Surface rips were seen above the descending limb of the internal waves cellular flow structure.

Apel *et al.* (1985) placed three current meter moorings at varying distances from the origin point of the surface lineations seen by satellites in the Sulu Sea, and conducted an extensive ship-board profiling program. The mooring data was dominated by the semidiurnal tide, but large spikes associated with internal wave packets also occurred as the ebb tide turned to flood. The amplitude of these groups was heavily modulated by the 14 day spring tide cycle. The waves existed as depressions of the thermocline with amplitudes to 90 m and were rank-ordered and well-formed at the leading edge. The wave trains were superimposed on a broad thermocline depression of about 50 m amplitude and 6 h period. Near-surface velocities of up to 1 m/s were oriented in the packet's propagation direction, while the deeper water flowed in the opposite direction, and the turning point in this cellular flow was at about 200 m depth. Breaking surface waves were seen above the descending limb of individual packet elements with amplitudes of 0.5–1 m and zone widths of about 1 km. The mean wavelength within each group was 2.6 km, and coherent wave packets were seen to exist for up to 2.5 d from creation to break-up in shallow water.

A generation mechanism for internal wave packets by tidal flow across topographic features has been investigated theoretically by Lee and Beardsley (1974) and using laboratory models by Maxworthy (1979). While they differ in some details, the overall conclusions of these studies are similar. Figure 1 outlines the basic ideas. As the ebb tide proceeds, a lee wave field is generated behind the topographic ridge by the locally supercritical flow. The magnitude of the lee wave field depends on a variety of factors, including the shape and height of the ridge, the water velocity, and the stratification of the water column. As the ebb tide slackens and turns to flood, the lee wave depression, which has developed a substantial phase velocity in order to remain stationary in the flow, begins to move upstream against the tide. As the front continues to propagate away from the ridge, it evolves into a series of solitary internal waves due to the effects of non-linearity and dispersion. The size and number of these waves depends in a complex way on local properties of the water column and on seafloor topography.

### Hydrodynamic Theory

The observational data reviewed earlier indicate that internal wave packets are nonlinear; the key evidence for this is the higher velocity of the longer wavelength components, as suggested by the presence of the longest wavelengths at the leading edge of any given group. In most instances, the individual wavelengths are at least of the order of the water depth. This means that the appropriate physics is that for nonlinear waves in a stratified medium under the long wave approximation.

The theory for nonlinear, long, internal waves is reviewed by Osborne and Burch (1980), Apel and Gonzalez (1983), and Fu and Holt (1984). For a two-dimensional  $(x, z)$  wave field (with  $z$  positive upwards and zero at the sea surface), the displacement field  $A(x, z, t)$  may be written

$$A(x, z, t) = \eta(x, t) \phi(z) \quad (1)$$

where  $\eta(x, t)$  describes the horizontal structure and  $\phi(z)$  is a dimensionless vertical mode function which is normalized so that its maximum value is unity. For waves with long horizontal scales  $L$  and small (but finite) amplitudes  $\eta$  in water of depth  $H$ , such that  $H/L$  and  $\eta/H$  are small compared to unity, perturbation methods (e.g., Benny, 1966; Whitham, 1974) may be used

to get relatively simple equations for  $\eta$  and  $\phi$ . The lowest order vertical mode equation is the familiar linear one for internal waves

$$\partial_z^2 \phi - \frac{N^2(z)}{c_0^2} \phi = 0 \quad (2)$$

together with

$$\phi(0) = \phi(-H) = 0 \quad (3)$$

where  $N(z)$  is the Brunt-Väisälä or buoyancy profile of the water column and  $c_0$  is the eigenvalue of (1), which corresponds to the phase velocity of long, linear internal waves. This equation is valid for frequencies which are large compared to the local inertial frequency, but small relative to the buoyancy frequency.

The zeroth order equation for the horizontal structure function is the Korteweg-deVries equation (Whitham, 1974)

$$\partial_t \eta - c_0 \partial_x \eta - \alpha \eta \partial_x \eta - \gamma \partial_x^3 \eta = 0 \quad (4)$$

The environmental parameters  $\alpha$  and  $\gamma$  depend on the buoyancy profile  $N(z)$  and the vertical eigenfunctions  $\phi$ , such that

$$\alpha = \frac{-c_0 \int_{-H}^0 dz \partial_z N^2(z) \phi^2(z)}{\int_{-H}^0 dz N^2(z) \phi^2(z)} \quad (5)$$

$$\gamma = \frac{c_0^3 \int_{-H}^0 dz \phi^2(z)}{2 \int_{-H}^0 dz N^2(z) \phi^2(z)} \quad (6)$$

Apel and Gonzalez [1983] give a physical interpretation of these quantities. The nonlinear parameter  $\alpha$  is a measure of the degree of amplitude "stickiness" or the degree with which a finite amplitude wave travels faster than its nonlinear counterpart. This is caused by the fact that a finite amplitude wave perturbs the local density structure significantly, altering the local dynamics. The coefficient  $\gamma$  is a measure of the importance of physical dispersion, and  $\gamma^{-1/2}$  is the wavenumber at which a quadratic approximation to the dispersion relation vanishes.

There are a number of steady-state solutions of (4) that are possible when the nonlinear and dispersive terms balance. The simplest one is the long-wavelength internal soliton. For water that is deep compared to the vertical scale of the thermocline, the only soliton solution that is possible is one of depression given by

$$\eta(x,t) = -\eta_c \operatorname{sech}^2\left(\frac{x-ct}{L}\right) \quad (7)$$

where  $c$  is its nonlinear phase speed and  $L$  is a measure of its width. These are related by

$$c = c_c \left(1 + \frac{\eta_c \alpha}{3c_c}\right) \quad (8)$$

$$\eta_c = \frac{3c_c}{\alpha} \left(1 - \frac{c}{c_0}\right) \quad (9)$$

$$L = \sqrt{\frac{12\gamma}{\eta_c \alpha}} \quad (10)$$

The soliton solution (7) consists of a single, bell-shaped depression of the thermocline, and is a reasonable approximation to a single element of an internal wave packet. The importance of the soliton solution lies in its behavior, including 1) the soliton phase speed (8) exceeds the linear phase speed  $c_c$  by an amount that is proportional to its amplitude  $\eta_c$ , 2) since larger solitons travel faster, packets of them will evolve into rank-ordered groups with the largest elements at the front, 3) interacting solitons experience at most a phase shift, retaining their original velocities and shapes after collision, and 4) since individual solitons evolve with independent sizes and phase velocities, the distance between individual solitons in a packet is a measure of the distance of propagation from the source. These properties are all consistent with the observed characteristics of internal wave packets. Other soliton rules are reviewed by Osborne and Burch 1980. Note that internal wave groups may be regarded as superpositions of solitons (7) of different amplitudes, and hence different velocities.

A second steady-state solution of (4) is reviewed by Apel and Gonzalez [1983] and is called the cnoidal solution with

$$\eta(x,t) = \eta_m - \eta_0 c n_m^2\left(\frac{x-ct}{L}\right) \quad (11)$$

where  $cn_m$  is one of the Jacobi elliptic functions. This wave also propagates without change of shape and consists of an infinite series of negative troughs of amplitude  $\eta_c$ . The cnoidal solution is a nonlinear generalization of the cosine, and reduces to that form in the linear limit. While Apel and Gonzalez (1983) used this solution to model observed internal wave packets, it will not be considered further in this report due to its analytic complexity.

To compute the environmental parameters (5)–(6), it is necessary to have a good estimate of the buoyancy frequency profile  $N(z)$ . This may not be available *in-situ*, particularly when the data consists only of satellite imagery. While the vertical structure equation (2) has an infinite number of eigensolutions corresponding to the different vertical modes, observational data suggests that only the lowest order one, having a single maximum at mid-depths, is actually present (Ziegenbein, 1969, 1970; Halpern, 1971; Osborne and Burch, 1980). This means that numerical solution of (2)–(3) for the first mode together with numerical evaluation of (5)–(6) can allow realistic approximations to be made with the internal soliton model, commensurate with the available knowledge about  $N(z)$ . This procedure was used by Fu and Holt (1984), although their buoyancy profile data consisted only of historical averages rather than synoptic measurements.

Instead of using this relatively complex procedure, and in view of the many other approximations that go into the internal soliton model (7), the simple two-layer model of Osborne and Burch (1980) will be adopted. This will allow analytical expressions for the electromagnetic fields to be derived, consistent with a philosophy of simplicity in which order-of-magnitude estimates for the internal wave magnetic fields are sought. In a two-layer ocean model, only the lowest order vertical mode is possible, and the vertical structure function in (2) is approximated by straight line segments. For an upper layer of thickness  $h_1$  and density  $\rho_1$  overlying a lower layer of thickness  $h_2$  and density  $\rho_2$ , where  $h_1 < h_2$  so that (7) is valid, the environmental parameters (5)–(6) and the linear phase velocity  $c_0$  are given by [Osborne and Burch, 1980]

$$\alpha \approx \frac{-3c_0(h_1 - h_2)}{2h_1h_2} \quad (12)$$

$$\gamma \approx \frac{c_0h_1h_2}{6} \quad (13)$$

$$c_0 \approx \sqrt{\frac{g\Delta\rho h_1h_2}{\rho(h_1 - h_2)}} \quad (14)$$

where  $\rho \approx \rho_1 \approx \rho_2$  and  $\Delta\rho = \rho_2 - \rho_1$ . The horizontal water velocities in the two layers are

$$u_1(x, t) = \frac{c_0\eta_0}{h_1} \operatorname{sech}^2 \xi \quad (15)$$

$$u_2(x, t) = -\frac{c_0\eta_0}{h_2} \operatorname{sech}^2 \xi \quad (16)$$

where

$$\xi = \frac{x - ct}{L} \quad (17)$$

Note that the horizontal velocity components are depth-independent within a given layer but discontinuous at the thermocline  $z = -h_1$ , and that they have opposite directions in the different layers. The vertical velocity components follow from the continuity equation and the rigid lid approximation

$$\begin{aligned} w_1(x, z, t) &= -(\partial_x u_1(x, t))z \\ &= \frac{2c_0\eta_0 z}{h_1 L} \operatorname{sech}^2 \xi \tanh \xi \end{aligned} \quad (18)$$

$$\begin{aligned} w_2(x, z, t) &= -(\partial_x u_2(x, t))(z - H) \\ &= -\frac{2c_0\eta_0(z - H)}{h_2 L} \operatorname{sech}^2 \xi \tanh \xi \end{aligned} \quad (19)$$

Note that  $w_1 = w_2$  at the thermocline  $z = -h_1$ , and that the vertical velocity depends linearly on the depth with a maximum value at the interface. The water motion is prograde elliptical, with the upper layer water moving in the direction of wave propagation, descending at the leading edge of the soliton, and rising at its trailing edge. A small surface soliton accompanies the internal one, and is neglected in this treatment. Figure 2 illustrates the geometry and soliton

behavior of the model.

### Electromagnetic Theory

The framework for the theory of electromagnetic induction used in this report is similar to that in Chave 1984. The Maxwell equations in the quasistatic limit, in which the magnetic effects of the displacement current are neglected, govern the electromagnetic fields

$$\nabla \cdot \vec{B} = 0 \quad (20)$$

$$\nabla \times \vec{E} + \sigma_1 \vec{B} = 0 \quad (21)$$

$$\vec{B} = \mu \sigma \vec{E} + \mu \vec{J}^0 \quad (22)$$

where  $\vec{E}$  is the electric field,  $\vec{B}$  is the magnetic induction,  $\mu$  is the magnetic permeability of free space,  $\sigma$  is the electrical conductivity, and  $\vec{J}^0$  is a specified, impressed source electric current density. For induction processes that are driven by moving seawater, the latter is given by

$$\vec{J}^0 = \sigma_0 (\vec{v} \times \vec{F}) \quad (23)$$

where  $\sigma_0$  is the conductivity of seawater,  $\vec{v}$  is the water velocity, and  $\vec{F}$  is the geomagnetic induction, assumed sourceless, curl-free, and time invariant. Replacement of  $\vec{B}$  with  $\vec{F}$  in (23) linearizes the set (20)–(23) by eliminating the effect of feedback by the induced magnetic field on the velocity field.

Solutions of (20)–(23) will be sought using potentials in a Cartesian coordinate system. By virtue of (20), the magnetic induction may be written

$$\vec{B} = \nabla \times (\Pi \hat{z}) + \nabla_h \partial_z \Psi - \nabla_h^2 \Psi \quad (24)$$

where  $\Pi$  and  $\Psi$  are scalar functions which represent the toroidal and poloidal magnetic (TM and PM) parts of the magnetic field and  $\nabla_h$  is the horizontal derivative operator  $\partial_x \hat{x} + \partial_y \hat{y}$ . The source current in (22)–(23) may also be expressed in terms of scalar functions

$$\vec{J}^0 = \Xi \hat{z} + \nabla_h T + \nabla \times (\Upsilon \hat{z}) \quad (25)$$

where  $T$  and  $\Upsilon$  satisfy

$$\nabla_h^2 T = \sigma_0 (\nabla_h \times \vec{v}_h \cdot \vec{F}_z \hat{z} + \sigma_0 (\nabla_h \times \vec{v}_z \hat{z}) \cdot \vec{F}_h) \quad (26)$$

$$\nabla_h^2 \Upsilon = \sigma_0 (\nabla_h \cdot \bar{F}_h) F_z - \sigma_0 (\bar{F}_h \cdot \nabla_h) \Upsilon_z \quad (27)$$

and

$$\Xi = \sigma_0 (\bar{F}_h \cdot \bar{F}_h) \cdot \hat{z} \quad (28)$$

Spatial variations of  $\bar{F}$  have been neglected in (26)–(27), consistent with the study of small-scale oceanic phenomena.

If  $\sigma$  is assumed to be a function of depth, uncoupled partial differential equations for  $\Pi$  and  $\Psi$  may be obtained by writing the electric field in a form like (25), substituting into (21)–(22), writing out the Cartesian components, and applying complex variable theory to the result, yielding

$$\nabla_h^2 \Pi - \sigma \partial_z (\partial_z \Pi / \sigma) - \mu \sigma \partial_t \Pi = -\mu \Xi - \mu \sigma \partial_z (T \sigma) \quad (29)$$

$$\nabla_h^2 \Psi - \mu \sigma \partial_t \Psi = -\mu \Upsilon \quad (30)$$

where

$$\bar{E} = -\nabla_h^2 \Pi / \mu - \Xi / \sigma \hat{z} - \nabla_h (\partial_z \Pi / \mu - T \sigma) - \nabla_h (\partial_t \Psi \hat{z}) \quad (31)$$

Independence of the TM and PM modes is assured because the usual electromagnetic boundary conditions at horizontal interfaces are decoupled.

It is especially convenient to solve (29)–(30) by expressing the time variable ( $e^{-i\omega t}$  convention) and the horizontal coordinates as Fourier transforms using the standard pair

$$\begin{aligned} f(k, l) &= \int_{-\infty}^{\infty} \int_{-\infty}^{\infty} dx dy e^{i(kx + ly)} f(x, y) \\ f(x, y) &= \frac{1}{(2\pi)^2} \int_{-\infty}^{\infty} \int_{-\infty}^{\infty} dk dl e^{-i(kx + ly)} f(k, l) \end{aligned} \quad (32)$$

Green functions for (29)–(30) may then be found for a constant depth ocean of uniform conductivity, where

$$\hat{\Pi}(k, l, z) = -\mu \int_{-H}^0 dz' g_{\pi}(z, z') \hat{\Xi}(z') - \mu \int_{-H}^0 dz' \partial_z g_{\pi}(z, z') \hat{T}(z') \quad (33)$$

$$\hat{\Psi}(k, l, z) = -\mu \int_{-H}^0 dz' g_{\psi}(z, z') \hat{\Upsilon}(z') \quad (34)$$



and

$$g_{\Pi}(z, z') = - \frac{e^{-\beta_0(z-z')} - R_L^{TM} e^{-2\beta_0 H} e^{-\beta_0(z+z')} - e^{\beta_0(z-z')} R_L^{TM} e^{-2\beta_0 H} e^{\beta_0(z+z')}}{2\beta_0(1 - R_L^{TM} e^{-2\beta_0 H})} \quad (35)$$

$$g_{\Psi}(z, z') = - \frac{e^{-\beta_0(z-z')} - R_L^{PM} e^{-2\beta_0 H} e^{-\beta_0(z+z')} - R_A^{PM} e^{\beta_0(z+z')} - R_A^{PM} R_L^{PM} e^{-2\beta_0 H} e^{\beta_0(z-z')}}{2\beta_0(1 - R_A^{PM} R_L^{PM} e^{-2\beta_0 H})} \quad (36)$$

The induction parameter is

$$\beta = \sqrt{k^2 - l^2 - i\omega\mu\sigma(z)} \quad (37)$$

with  $\beta_0$  given when  $\sigma(z) = \sigma_0$ , while the modal reflection coefficients are

$$R_L^{TM} = \frac{\frac{\beta_0 K}{\sigma_1} - 1}{\frac{\beta_0 K}{\sigma_0} - 1} \quad (38)$$

$$R_L^{PM} = \frac{\beta_0 \Lambda - 1}{\beta_0 \Lambda + 1} \quad (39)$$

$$R_A^{PM} = \frac{\beta_0 - \sqrt{k^2 - l^2}}{\beta_0 + \sqrt{k^2 - l^2}} \quad (40)$$

Expressions for the modal response functions K and  $\Lambda$  may be found in Chave and Cox [1982] for a layered medium. For the purposes of this report, only a halfspace of uniform conductivity  $\sigma_1$  will be considered, reducing (38)–(39) to

$$R_L^{TM} = \frac{\beta_0 \sigma_1 - \beta_1 \sigma_0}{\beta_0 \sigma_1 + \beta_1 \sigma_0} \quad (41)$$

$$R_L^{PM} = \frac{\beta_0 - \beta_1}{\beta_0 + \beta_1} \quad (42)$$

### The Internal Soliton Electromagnetic Fields – Theory

The electromagnetic fields may be found by Fourier transforming (15)–(16), (18)–(19), and (26)–(28) to get expressions for the source current scalars, evaluating (33)–(34) to get the electromagnetic scalar functions  $\hat{\Pi}$  and  $\hat{\Psi}$ , taking the inverse Fourier transform, and using (24) and (31). Using the Fourier transform identity

$$\int_{-\infty}^{\infty} dk e^{ikz} \operatorname{sech}^2 \xi = \pi L^2 k \operatorname{csch}\left(\frac{\pi kL}{2}\right) e^{ikct} \quad (43)$$

yields

$$\hat{T}_1(z, t) = \pi \sigma_0 F_y a_1 L^2 k z \operatorname{csch}\left(\frac{\pi kL}{2}\right) e^{ikct} \quad (44)$$

$$\hat{T}_2(z, t) = -\pi \sigma_0 F_y a_2 L^2 k (z - H) \operatorname{csch}\left(\frac{\pi kL}{2}\right) e^{ikct} \quad (45)$$

$$\hat{Y}_1(z, t) = \pi \sigma_0 L^2 a_1 \operatorname{csch}\left(\frac{\pi kL}{2}\right) e^{ikct} (F_x k z + i F_z) \quad (46)$$

$$\hat{Y}_2(z, t) = -\pi \sigma_0 L^2 a_2 \operatorname{csch}\left(\frac{\pi kL}{2}\right) e^{ikct} (F_x k (z - H) - i F_z) \quad (47)$$

$$\hat{\Xi}_1(z, t) = \pi \sigma_0 F_x a_1 k L^2 \operatorname{csch}\left(\frac{\pi kL}{2}\right) e^{ikct} \quad (48)$$

$$\hat{\Xi}_2(z, t) = -\pi \sigma_0 F_x a_2 k L^2 \operatorname{csch}\left(\frac{\pi kL}{2}\right) e^{ikct} \quad (49)$$

where  $a_1 = c_0 \eta_0 h_1$  and  $a_2 = c_0 \eta_0 h_2$

Rewriting the TM mode expression (33) by integrating the second term by parts, it is easy to show that the induced part of the TM mode electric field and the TM mode magnetic field vanish if  $\hat{\Xi} - \partial_z \hat{T} = 0$  and  $\hat{T}(-H) = 0$ . Using (44)-(45) and (48)-(49), it is clear that these conditions hold, and the TM mode need not be considered further. From (31), there is a remaining TM mode electric component given by

$$\bar{E}^{TM} = -\frac{\hat{\Xi}}{\sigma_0} \hat{z} - \frac{\nabla_{\perp} T}{\sigma_0} \quad (50)$$

This is just the quasistatic electric field required to ensure that no electric current is associated with this mode, and that no current flows in the  $x-z$  plane.

The remaining, PM mode, electromagnetic problem is most easily solved by writing (46)-(47) as the sum of parts due to  $F_x$  and  $F_z$  induction. Taking the Fourier transform in time, this gives

$$\hat{Y}_1^z(z) = 2\pi^2 \sigma_0 F_x L^2 a_1 k z \operatorname{csch}\left(\frac{\pi kL}{2}\right) \delta(\omega - kc) \quad (51)$$

$$\hat{Y}_2^z(z) = -2\pi^2 \sigma_0 F_x L^2 a_2 k (z + H) \operatorname{csch}\left(\frac{\pi kL}{2}\right) \delta(\omega - kc) \quad (52)$$

$$\hat{Y}_1^z(z) = i 2\pi^2 \sigma_0 F_z L^2 a_1 \operatorname{csch}\left(\frac{\pi kL}{2}\right) \delta(\omega - kc) \quad (53)$$

$$\hat{Y}_2^z(z) = -i 2\pi^2 \sigma_0 F_z L^2 a_2 \operatorname{csch}\left(\frac{\pi kL}{2}\right) \delta(\omega - kc) \quad (54)$$

where  $\delta(x)$  is the Dirac delta function. Owing to the linearity of the Maxwell equations, the two parts of the PM mode scalar  $\hat{\Psi}$  due to (51)–(52) and (53)–(54) may be computed separately and then combined.

The interest in this report is confined to the magnetic field at or above the sea surface ( $z = 0$ ) and at the seafloor ( $z = -H$ ). From (24), there are four Green functions that are required

$$g_\Psi(0, z') = - \frac{(R_A^{PM} - 1)(e^{\beta_0 z'} + R_L^{PM} e^{-2\beta_0 H} e^{-\beta_0 z'})}{2\beta_0(1 - R_A^{PM} R_L^{PM} e^{-2\beta_0 H})} \quad (55)$$

$$\partial_z g_\Psi(0, z') = - \frac{(R_A^{PM} - 1)(e^{\beta_0 z'} - R_L^{PM} e^{-2\beta_0 H} e^{-\beta_0 z'})}{2(1 - R_A^{PM} R_L^{PM} e^{-2\beta_0 H})} \quad (56)$$

$$g_\Psi(-H, z') = \frac{e^{-\beta_0 H} (R_L^{PM} - 1)(e^{\beta_0 z'} - R_A^{PM} e^{-\beta_0 z'})}{2\beta_0(1 - R_A^{PM} R_L^{PM} e^{-2\beta_0 H})} \quad (57)$$

$$\partial_z g_\Psi(-H, z') = \frac{e^{-\beta_0 H} (R_L^{PM} - 1)(e^{-\beta_0 z'} - R_A^{PM} e^{\beta_0 z'})}{2(1 - R_A^{PM} R_L^{PM} e^{-2\beta_0 H})} \quad (58)$$

Combining (51)–(52) with (55)–(56), evaluating (34), and taking the inverse Fourier transforms of the  $x$  and  $t$  variables yields

$$\Psi^z(0) = \frac{\mu \sigma_0 F_z L^2}{4} \int_{-\infty}^{\infty} dk e^{-ikL\epsilon} \frac{k \operatorname{csch}\left(\frac{\pi kL}{2}\right) (R_A^{PM} + 1)(a_1 A_1 - a_2 A_2)}{\beta_0(1 - R_A^{PM} R_L^{PM} e^{-2\beta_0 H})} \quad (59)$$

$$\partial_z \Psi^z(0) = \frac{\mu \sigma_0 F_z L^2}{4} \int_{-\infty}^{\infty} dk e^{-ikL\epsilon} \frac{k \operatorname{csch}\left(\frac{\pi kL}{2}\right) (R_A^{PM} - 1)(a_1 A_1 - a_2 A_2)}{1 - R_A^{PM} R_L^{PM} e^{-2\beta_0 H}} \quad (60)$$

where  $\beta_1 = \sqrt{k^2 - ikc\mu\sigma}$ , in (39)–(40) and

$$A_1 = \left[ \left( (\beta_0 h_1 + 1) - R_L^{PM}(\beta_0 h_1 - 1)e^{-2\beta_0 h_1} \right) e^{-\beta_0 h_1} - (R_L^{PM} e^{-2\beta_0 H} + 1) \right] / \beta_0^2$$

$$A_2 = \left[ \left( (\beta_0 h_2 - 1) - R_L^{PM}(\beta_0 h_2 + 1)e^{-2\beta_0 h_2} \right) e^{-\beta_0 h_2} + (R_L^{PM} + 1)e^{-\beta_0 H} \right] / \beta_0^2$$

Applying (24) gives the  $x$ - and  $z$ -components of the magnetic fields at the sea surface. To get the magnetic fields above the sea surface, note that in air and in the absence of sources,  $\Psi$  obeys a one-dimensional homogeneous Helmholtz equation, vanishes as  $z \rightarrow \infty$ , and is specified on  $z = 0$ , so that

$$\Psi(z) = \Psi(0)e^{-kz} \quad (61)$$

The airborne magnetic fields follow by taking the appropriate derivatives of (59) after multiplying the kernel by  $e^{-kz}$ , yielding

$$B_z^x(z) = \frac{i\mu\sigma_0 F_z L^2}{4} \int_{-\infty}^{\infty} dk e^{-ikL\xi} \frac{e^{-\alpha z} k^2 \alpha \operatorname{csch}(\frac{\pi kL}{2})(R_A^{PM}-1)(a_1 A_1 - a_2 A_2)}{\beta_0(1-R_A^{PM}R_L^{PM}e^{-2\beta_0 H})} \quad (62)$$

$$B_z^z(z) = \frac{\mu\sigma_0 F_z L^2}{4} \int_{-\infty}^{\infty} dk e^{-ikL\xi} \frac{e^{-\alpha z} k^3 \operatorname{csch}(\frac{\pi kL}{2})(R_A^{PM}-1)(a_1 A_1 - a_2 A_2)}{\beta_0(1-R_A^{PM}R_L^{PM}e^{-2\beta_0 H})} \quad (63)$$

where  $\alpha = k$ . Note that (62) reduces to the  $x$ -derivative of (60) when  $z \rightarrow 0$ .

A similar procedure gives the  $F_z$  induction part of the magnetic fields at and above the sea surface

$$\Psi^z(0) = \frac{i\mu\sigma_0 F_z L^2}{4} \int_{-\infty}^{\infty} dk e^{-ikL\xi} \frac{\operatorname{csch}(\frac{\pi kL}{2})(R_A^{PM}-1)(a_1 B_1 - a_2 B_2)}{\beta_0(1-R_A^{PM}R_L^{PM}e^{-2\beta_0 H})} \quad (64)$$

$$\partial_z \Psi^z(0) = \frac{i\mu\sigma_0 F_z L^2}{4} \int_{-\infty}^{\infty} dk e^{-ikL\xi} \frac{\operatorname{csch}(\frac{\pi kL}{2})(R_A^{PM}-1)(a_1 B_1 - a_2 B_2)}{1-R_A^{PM}R_L^{PM}e^{-2\beta_0 H}} \quad (65)$$

$$B_z^x(z) = -\frac{\mu\sigma_0 F_z L^2}{4} \int_{-\infty}^{\infty} dk e^{-ikL\xi} \frac{k\alpha e^{-\alpha z} \operatorname{csch}(\frac{\pi kL}{2})(R_A^{PM}-1)(a_1 B_1 - a_2 B_2)}{\beta_0(1-R_A^{PM}R_L^{PM}e^{-2\beta_0 H})} \quad (66)$$

$$B_z^z(z) = \frac{i\mu\sigma_0 F_z L^2}{4} \int_{-\infty}^{\infty} dk e^{-ikL\xi} \frac{k^2 e^{-\alpha z} \operatorname{csch}(\frac{\pi kL}{2})(R_A^{PM}-1)(a_1 B_1 - a_2 B_2)}{\beta_0(1-R_A^{PM}R_L^{PM}e^{-2\beta_0 H})} \quad (67)$$

where

$$B_1 = (1 - e^{-\beta_0 h_1})(1 + R_L^{PM}e^{-\beta_0 H}e^{-\beta_0 h_2})/\beta_0$$

$$B_2 = e^{-\beta_0 h_1}(1 - e^{-\beta_0 h_2})(1 + R_L^{PM}e^{-\beta_0 H}e^{-\beta_0 h_2})/\beta_0$$

The magnetic fields at the seafloor are obtained in an identical manner. For induction by the  $F_z$  geomagnetic field, they are

$$B_z^s(-H) = \frac{-i\mu\sigma_0 F_z L^2}{4} \int_{-\infty}^{\infty} dk e^{-ikL\xi} \frac{k^2 \operatorname{csch}\left(\frac{\pi kL}{2}\right) (R_L^{PM}-1)(a_1 C_1 - a_2 C_2)}{1 - R_A^{PM} R_L^{PM} e^{-2\beta_0 H}} \quad (68)$$

$$B_z^s(-H) = \frac{\mu\sigma_0 F_z L^2}{4} \int_{-\infty}^{\infty} dk e^{-ikL\xi} \frac{k^2 \operatorname{csch}\left(\frac{\pi kL}{2}\right) (R_L^{PM}+1)(a_1 C_1 - a_2 C_2)}{\beta_0 (1 - R_A^{PM} R_L^{PM} e^{-2\beta_0 H})} \quad (69)$$

where

$$C_1 = [R_A^{PM}(\beta_0 h_1 - 1)e^{-2\beta_0 h_1} - (\beta_0 h_1 - 1)e^{-\beta_0 h_2} - (R_A^{PM} - 1)e^{-\beta_0 H}] / \beta_0^2$$

$$C_2 = [R_A^{PM}(\beta_0 h_2 - 1)e^{-2\beta_0 h_1} - (\beta_0 h_2 - 1)e^{-\beta_0 h_2} - (R_A^{PM} - 1)e^{-\beta_0 H}] / \beta_0^2$$

and for induction by the  $F_x$  geomagnetic field, they are

$$B_z^s(-H) = \frac{\mu\sigma_0 F_x L^2}{4} \int_{-\infty}^{\infty} dk e^{ikL\xi} \frac{k \operatorname{csch}\left(\frac{\pi kL}{2}\right) (R_L^{PM}-1)(a_1 D_1 - a_2 D_2)}{1 - R_A^{PM} R_L^{PM} e^{-2\beta_0 H}} \quad (70)$$

$$B_z^s(-H) = \frac{i\mu\sigma_0 F_x L^2}{4} \int_{-\infty}^{\infty} dk e^{ikL\xi} \frac{k^2 \operatorname{csch}\left(\frac{\pi kL}{2}\right) (R_L^{PM}+1)(a_1 D_1 - a_2 D_2)}{\beta_0 (1 - R_A^{PM} R_L^{PM} e^{-2\beta_0 H})} \quad (71)$$

where

$$D_1 = e^{-\beta_0 h_2} (1 - e^{-\beta_0 h_1}) (1 - R_A^{PM} e^{-\beta_0 h_1}) / \beta_0$$

$$D_2 = (1 - e^{-\beta_0 h_2}) (1 - R_A^{PM} e^{-\beta_0 H} e^{-\beta_0 h_1}) / \beta_0$$

The field component expressions (62)–(63) and (66)–(71) are easily evaluated using a fast Fourier transform algorithm. Care must be taken to ensure that the result is properly normalized, so that

$$\frac{1}{2\pi} \int_{-\infty}^{\infty} dk e^{-ikx} \hat{f}(k) \approx \frac{1}{N} \sum_{j=0}^{N-1} \hat{f}(k_j) e^{\frac{-i2\pi j l}{N}} \quad l = 0, \dots, N-1 \quad (72)$$

Note also that the magnetic fields display even or odd symmetry about  $\xi = 0$ , and can also be written as cosine or sine transforms.

### The Internal Soliton Electromagnetic Fields – Examples

In order to assess the size and spatial scales of the internal soliton magnetic fields both above the sea surface and at the seafloor, it is necessary to measure or estimate the hydrodynamic

quantities in (62)–(63) and (66)–(71). Due to the wide variety of settings in which these internal wave packets are observed, and the concomitant range of the relevant parameters, three examples were selected that span the range of soliton scales that seem to occur in nature. The first of these is from the Andaman Sea experiment of Osborne and Burch (1980), in which *in situ* measurements of the water velocity, stratification, and soliton length scales are available. The even larger internal wave packets seen in the Sulu Sea were excluded because the simple shallow-water soliton model is not strictly applicable (Apel *et al.*, 1985). The second example is taken from the satellite observations of Fu and Holt (1984) in the Gulf of California. While no *in situ* measurements are available at this site, the study is thorough, the water depth is typical of the outer continental shelf, and it is located at mid-latitudes. The final example is drawn from the Massachusetts Bay experiment of Halpern (1971), and is believed to be representative of shallow water and small soliton scales. Table 1 lists the water depths  $h_1$  and  $h_2$  for the two-layer soliton model, the soliton amplitude  $\eta_0$ , the soliton half-width  $L$ , the layer water velocities  $a_1$  and  $a_2$ , and the nonlinear phase speeds that have been either measured or estimated for these three cases. Except for the Andaman Sea data, these values are quite crude, and probably not accurate to better than a factor of 2 to 4.

The internal soliton magnetic fields also depend on the geomagnetic field components  $F_x$  and  $F_z$ . A simple, axially-geocentric dipole model of the geomagnetic field was employed

$$\begin{aligned} F_N &= F_0 \cos \lambda \\ F_Z &= -2F_0 \sin \lambda \end{aligned} \quad (73)$$

where  $F_0 \approx 3.05 \times 10^4$  nT,  $\lambda$  is the geographic latitude given in Table 1, and  $F_N$  and  $F_Z$  are the north and vertical geomagnetic components. The errors associated with neglecting the off-center nature of the real geomagnetic field and ignoring its east-west component are small at low- to mid-latitudes. Note from (62)–(63) and (68)–(69) that the  $F_x$  field is the component of the geomagnetic field in the direction of soliton propagation. This means that a soliton will generate the largest possible magnetic field when traveling north, while one that is moving to the east will interact only with the vertical geomagnetic field, yielding a smaller anomaly. Note also that the components (66)–(67) and (70)–(71) are invariant under changes in the direction of soliton

propagation

Figures 3-6 show the four parts (62) (63) and (66) (67) of the magnetic field for the Anaman Sea data in Table 1 at and above the sea surface for a fixed time  $t$ . Since (62) and (67) can be written as sine and (63) and (66) as cosine transforms by taking advantage of the symmetries in their respective kernels, an antisymmetric form is expected for the first pair of fields and a symmetric one for the latter pair. This reflects the nature of the underlying driving electric currents, and can be understood by examining their spatial distribution. Transforming (51)-(54) back to the space and time domains gives

$$\Upsilon_1^z(x, z, t) = \sigma_0 F_z a_1 z \operatorname{sech}^2 \xi \quad (74)$$

$$\Upsilon_2^z(x, z, t) = -\sigma_0 F_z a_2 (z - H) \operatorname{sech}^2 \xi \quad (75)$$

$$\Upsilon_1^x(x, t) = \sigma_0 F_z a_1 L \tanh \xi \quad (76)$$

$$\Upsilon_2^x(x, t) = \sigma_0 F_z a_2 L \tanh \xi \quad (77)$$

Applying (25) gives the driving current density, which has a singlet component

$$J_z^0 = -\partial_z \Upsilon \quad (78)$$

The two layers denoted by the subscript may be considered separately, and have a similar but oppositely-directed effect. In the top layer, (74) gives an antisymmetric or odd source function about  $\xi = 0$  that may be thought of as due to a pair of opposing line currents on either side of  $\xi = 0$ . The horizontal magnetic field from such a current pair will also be antisymmetric and display relative peaks above each line source. This is seen in Figure 3. The vertical magnetic field will be symmetric and have its largest magnitude between the two line sources where the individual contributions add constructively. This is seen in Figure 4. The second part of the upper layer source current given by (76) has a symmetric or even functional dependence that may be thought of as due to a single line current at  $\xi = 0$ . The horizontal magnetic field from such a current is symmetric, while the vertical component is antisymmetric, accounting for the behavior in Figures 5 and 6. The contributions from the lower layer are similar but of opposite sign. For an observer located above the sea surface, the upper layer is dominant due to its proximity, and the oppositely-directed anomaly from the lower layer is broader and of lower amplitude. This is seen clearly in the wings that are apparent in Figure 4. An observer at the seafloor would be

more strongly affected by the lower layer. Note that the actual currents in (74)–(77) with (78) are extended in the  $x$ -direction, and also vary in the  $z$ -direction in the case of (74)–(75).

The soliton model is a propagating one, as seen in the argument  $\xi L$  in the complex exponential in (62)–(63) and (66)–(71). For an airborne observer, the sensor velocity  $u$  is much larger than the soliton phase velocity  $c$ , and time may be regarded as fixed while the sensor moves over the soliton. For a seafloor observer, the position  $x$  is fixed, and the time progression of the soliton will be seen.

Figures 7 and 8 show the horizontal and vertical magnetic fields for the Andaman Sea soliton propagating to the north, and are the sums of Figures 3 and 5 or 4 and 6, respectively. The purely symmetric anomalies of Figures 3–6 have now vanished. A soliton moving to the east would produce only the fields of Figures 5 and 6, since induction by the north geomagnetic field does not occur. The peak-to-peak amplitudes of the induced magnetic fields range from 0.5–3 nT, and are much larger in Figures 7 and 8 because the geomagnetic field is nearly horizontal at very low latitudes ( $F_z \ll F_N$ ). The anomaly wavelengths reflect the horizontal soliton scale  $L$ , in this case about 1 km. The magnetic fields are largest at the sea surface, and attenuate slowly with height until a distance comparable to the soliton scale is achieved, beyond which the fields vanish more rapidly. Note that the magnetic fields are only reduced by a factor of 2 at 500 m altitude. This could be contrasted with deep-ocean internal wave magnetic fields, which attenuate exponentially with height with a wavelength-dependent  $e$ -folding scale that does not exceed a few hundred meters. The difference in behavior is due to the localized, dipolar nature of the internal soliton sources, while the deep-ocean internal waves are due to an extended and random source.

While these results show the vector behavior of internal soliton magnetic fields, most airborne magnetometers measure only the scalar magnitude rather than the actual vector components. The anomaly seen by an absolute intensity instrument is equivalent to the projection of the induced magnetic field onto the local geomagnetic induction vector because the latter far exceeds the former in size and will dominate the measurements. The total field anomaly is given



by

$$B \approx \bar{B} + \frac{\bar{F}}{\bar{F}} \quad (79)$$

where  $\bar{B}$  is the internal soliton magnetic field (62)–(63) and (66)–(67) and  $\bar{F}$  is the geomagnetic field. As always, there are two limiting cases to be considered – a soliton traveling to the north, in which (62)–(63) contribute, and soliton moving to the east, in which only induction by the vertical force is important. Figures 9 and 10 illustrate these two situations. Since the geomagnetic field is nearly horizontal and north-directed at the latitude of the Andaman Sea, the north-moving soliton produces a sizable anomaly with a peak-to-peak amplitude of 3.5 nT at the sea surface. By way of contrast, an east-moving soliton gives an amplitude of only about 0.2 nT. The remaining behavior, and especially the attenuation with height, is like that in Figures 7 and 8.

Figures 11 and 12 illustrate the vector magnetic components for an internal soliton in the Gulf of California using the hydrodynamic parameters of Table 1 and moving to the north, as in Figures 7 and 8. The peak-to-peak amplitudes are about 1.5 nT at the sea surface, attenuating slowly with height until a distance comparable to the soliton scale  $L$  is reached. The horizontal scale of the magnetic field reflects the 300 m width of the model soliton. Figures 13 and 14 show the total field anomalies obtained from (79) for solitons traveling to the north and east. At this mid-latitude site, the horizontal and vertical geomagnetic fields are comparable in magnitude, and only shape differences are seen between the anomalies for the two directions of soliton propagation.

Figures 15 and 16 show the horizontal and vertical magnetic components for the Massachusetts Bay case in Table 1, again for a north-moving disturbance. Due to the very small (60 m) scale of the soliton, attenuation for heights above 100 m is severe. The surface peak-to-peak amplitude is about 0.5 nT for both the horizontal and vertical magnetic fields. Figures 17 and 18 give the total field anomalies for solitons propagating to the north and east respectively. The behavior is similar to that of the vector components and reflects the mid-latitude equipartition of the geomagnetic field into horizontal and vertical parts.

Figures 19-21 give the corresponding seafloor magnetic fields for the Andaman Sea, Gulf of California, and Massachusetts Bay models using (68)-(71) and assuming northward soliton propagation. In each case, the position  $x$  is arbitrarily set to zero and the time coordinate has been reversed to reflect the behavior that would actually be observed by a fixed observer. The fields are comparable in size to the sea surface values, while the time scales reflect the value of  $L/c$ , where  $L$  is the soliton scale and  $c$  the soliton phase velocity. These fields are quite large, especially when compared to the ambient ionospheric values at the periods of interest, and could be expected to contaminate seafloor geophysical data quite appreciably.

In closing, two additional observations must be made. First, these magnetic anomalies are nearly static in behavior, and induction in either the ocean or earth is negligible. While a fixed seafloor conductivity of  $0.005 \text{ S/m}$  was assumed, a change in this quantity by an order of magnitude does not alter the magnetic field by more than a few percent. The value of seawater conductivity (fixed at  $3.2 \text{ S/m}$ ) is only important in its effect on the magnitude of the source currents (74)-(77) with (78), and is well-known in any case. In a similar vein, the frequency  $\omega$  in (35)-(42) would ordinarily be replaced by the frequency-of-encounter  $kv$  for a sensor moving at a velocity  $v$  which is much larger than the phase velocity  $c$  of the soliton. This suggests that  $v$  should replace  $c$  in  $\beta_i$  in (62)-(63) and (66)-(71). Since induction is a small effect, this also does not alter the results in Figures 1-18 very much. This suggests that the Green functions (55)-(58) could be replaced with the whole space values without introducing a substantial amount of error, and could yield analytic values for the magnetic fields.

Finally, the models presented in this report are for an isolated soliton of depression. In the ocean, internal solitons occur in packets consisting of a series of rank-ordered solitons whose wavelengths and amplitudes decrease from its leading to its trailing edge. Fortunately, the Maxwell equations are linear, and a real internal wave packet could be modeled by superimposing the results of this report with suitable spatial offsets and changes in the soliton parameters.

# References

- Apel, J. R., H. M. Byrne, J. R. Proni, and R. L. Charnell. Observations of oceanic internal and surface waves from the Earth Resources Technology Satellite. *J. Geophys. Res.*, 80, 865-881, 1975a.
- Apel, J. R., J. R. Proni, H. M. Byrne, and R. L. Sellers. Near-simultaneous observations of intermittent internal waves on the continental shelf from ship and spacecraft. *Geophys. Res. Lett.*, 2, 128-131, 1975b.
- Apel, J. R., H. M. Byrne, J. R. Proni, and R. L. Sellers. A study of oceanic internal waves using satellite imagery and ship data. *Rem. Sens. Env.*, 5, 125-135, 1976.
- Apel, J. R., and F. J. Gonzalez. Nonlinear features of internal waves off Baja California as observed from the SEASAT imaging radar. *J. Geophys. Res.*, 88, 4459-4466, 1983.
- Apel, J. R., J. R. Holbrook, A. K. Liu, and J. J. Tsai. The Sulu Sea Internal Soliton Experiment. *J. Phys. Ocean.*, 15, 1625-1651, 1985.
- Beal, H. T., and J. T. Weaver. Calculations of magnetic variations induced by internal waves. *J. Geophys. Res.*, 75, 6846-6852, 1970.
- Benny, D. J., Long nonlinear waves in fluid flows. *J. Math. Phys.*, 45, 52-63, 1966.
- Chave, A. D., On the electromagnetic fields induced by oceanic internal waves. *J. Geophys. Res.*, 89, 10519-10528, 1984.
- Chave, A. D., and C. S. Cox. Controlled electromagnetic sources for measuring electrical conductivity beneath the oceans, 1. forward problem and model study. *J. Geophys. Res.*, 87, 5327-5338, 1982.
- Curtin, T. B., and C. N. K. Mooers. Observation and interpretation of a high-frequency internal wave packet and surface slick pattern. *J. Geophys. Res.*, 80, 882-894, 1975.
- Elachi, C., and J. R. Apel. Internal wave observations made with an airborne synthetic aperture imaging radar. *Geophys. Res. Lett.*, 3, 647-650, 1976.
- Ewing, G., Slicks, surface films, and internal waves, *J. Mar. Res.*, 9, 161-187, 1950.
- Fu, L.-L., and B. Holt. Internal waves in the Gulf of California: observations from a spaceborne

- radar. *J. Geophys. Res.*, **89**, 2053-2060, 1984.
- Gargett, A. E., Generation of internal waves in the Strait of Georgia, British Columbia. *Deep Sea Res.*, **28**, 17-32, 1976.
- Gargett, A. E., and B. A. Hughes, On the interaction of surface and internal waves. *J. Fluid Mech.*, **52**, 179-191, 1972.
- Garrett, C., and W. Munk, Space-time scales of internal waves. *Geophys. Fluid Dyn.*, **2**, 225-264, 1972.
- Garrett, C., and W. Munk, Internal waves in the ocean. *Ann. Rev. Fluid Mech.*, **11**, 339-369, 1979.
- Halpern, D., Observations on short-period internal waves in Massachusetts Bay. *J. Mar. Res.*, **29**, 116-132, 1971.
- Haury, L. R., M. G. Briscoe, and M. H. Orr, Tidally-generated internal wave packets in Massachusetts Bay, *Nature*, **278**, 312-317, 1979.
- Ingram, R. G., Internal wave observations off Isla Verde. *J. Mar. Res.*, **36**, 715-724, 1978.
- Lee, C.-Y., and R. C. Beardsley, The generation of long nonlinear internal waves in a weakly stratified shear flow. *J. Geophys. Res.*, **79**, 453-462, 1974.
- Maxworthy, T., A note on the internal solitary waves produced by tidal flow over a three-dimensional ridge. *J. Geophys. Res.*, **84**, 338-346, 1979.
- Osborne, A. R., and T. L. Burch, Internal solitons in the Andaman Sea. *Science*, **208**, 451-460, 1980.
- Perry, R. B., and G. R. Schimke, Large-amplitude internal waves observed off the northwest coast of Sumatra. *J. Geophys. Res.*, **70**, 2319-2324, 1965.
- Petersen, R. A., and K. A. Poehls, Model spectrum of magnetic induction caused by ambient internal waves. *J. Geophys. Res.*, **87**, 433-440, 1982.
- Podney, W., Electromagnetic fields generated by ocean waves. *J. Geophys. Res.*, **80**, 2977-2990, 1975.
- Sandstrom, H., and J. A. Elliot, Internal tide and solitons on the Scotian Shelf: a nutrient pump

at work. *J. Geophys. Res.*, **89**, 6415-6426, 1984.

Trask, R. P., and M. G. Briscoe. Detection of Massachusetts Bay internal waves by the synthetic aperture radar (SAR) on SEASAT. *J. Geophys. Res.*, **88**, 1789-1799, 1983.

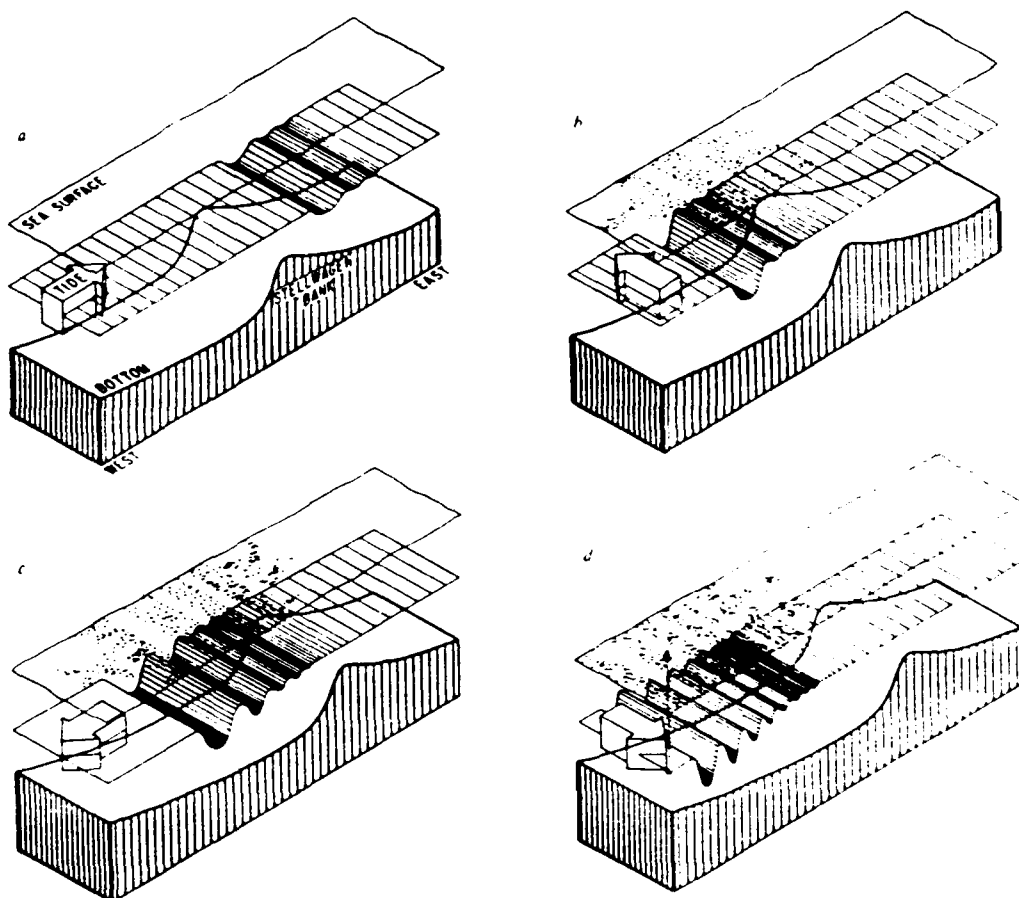
Whitham, G. B., *Linear and Nonlinear Waves*, 636pp., New York: John Wiley, 1974.

Ziegenbein, J., Short internal waves in the Strait of Gibraltar. *Deep Sea Res.*, **16**, 479-487, 1969.

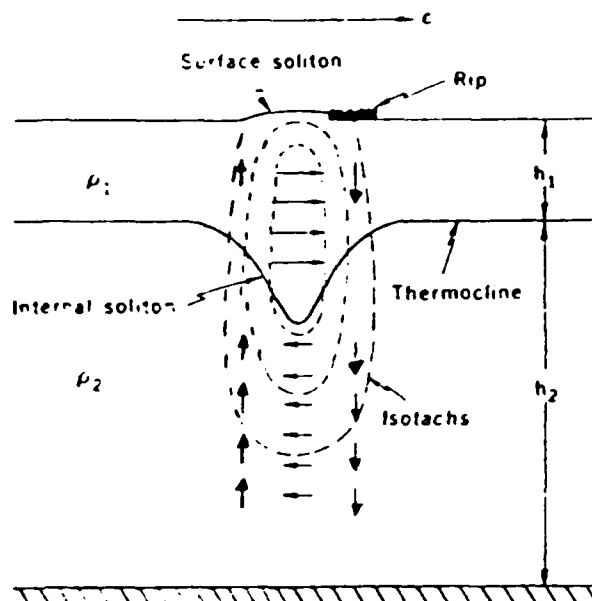
Ziegenbein, J., Spatial observations of short internal waves in the Strait of Gibraltar. *Deep Sea Res.*, **17**, 867-875, 1970.

Table 1. Internal Soliton Hydrodynamic Parameters

Parameter	Andaman Sea	Gulf of California	Massachusetts Bay
$h_1$ (meters)	230	50	17
$h_2$ (meters)	860	200	65
$H$ (meters)	1090	250	82
$\eta_c$ (meters)	60	50	10
$L$ (meters)	1200	300	60
$a_1$ (m s)	0.56	1.0	0.67
$a_2$ (m s)	0.15	0.25	0.18
$c$ (m s)	2.34	1.2	0.75
$\lambda$ (N)	7	29	42



**Figure 1.** Schematic diagram of internal wave packet generation as a lee wave during ebb tide (a), followed by nonlinear steepening of the lee wave depression (b) after the tide turns. The change in tidal flow direction allows the packet to propagate shorewards and over the bathymetric feature. Nonlinear and dispersive effects then allow undulations to develop behind the front in (c) and (d) (taken from Haury *et al.*, 1979).



**Figure 2.** Schematic diagram of an internal soliton on a two-layer fluid at finite depth. The soliton is a wave of depression, when the upper layer thickness  $h_1$  is smaller than the lower layer thickness  $h_2$ . The dashed lines are locii of constant water velocity (isotachs), while the arrows indicate the magnitude and direction of water flow. A small surface soliton accompanies the internal one, and surface rips are observed above the descending limb.



*Andaman Sea  $B_x^z$  at 0, .1, .5, and 1 km*

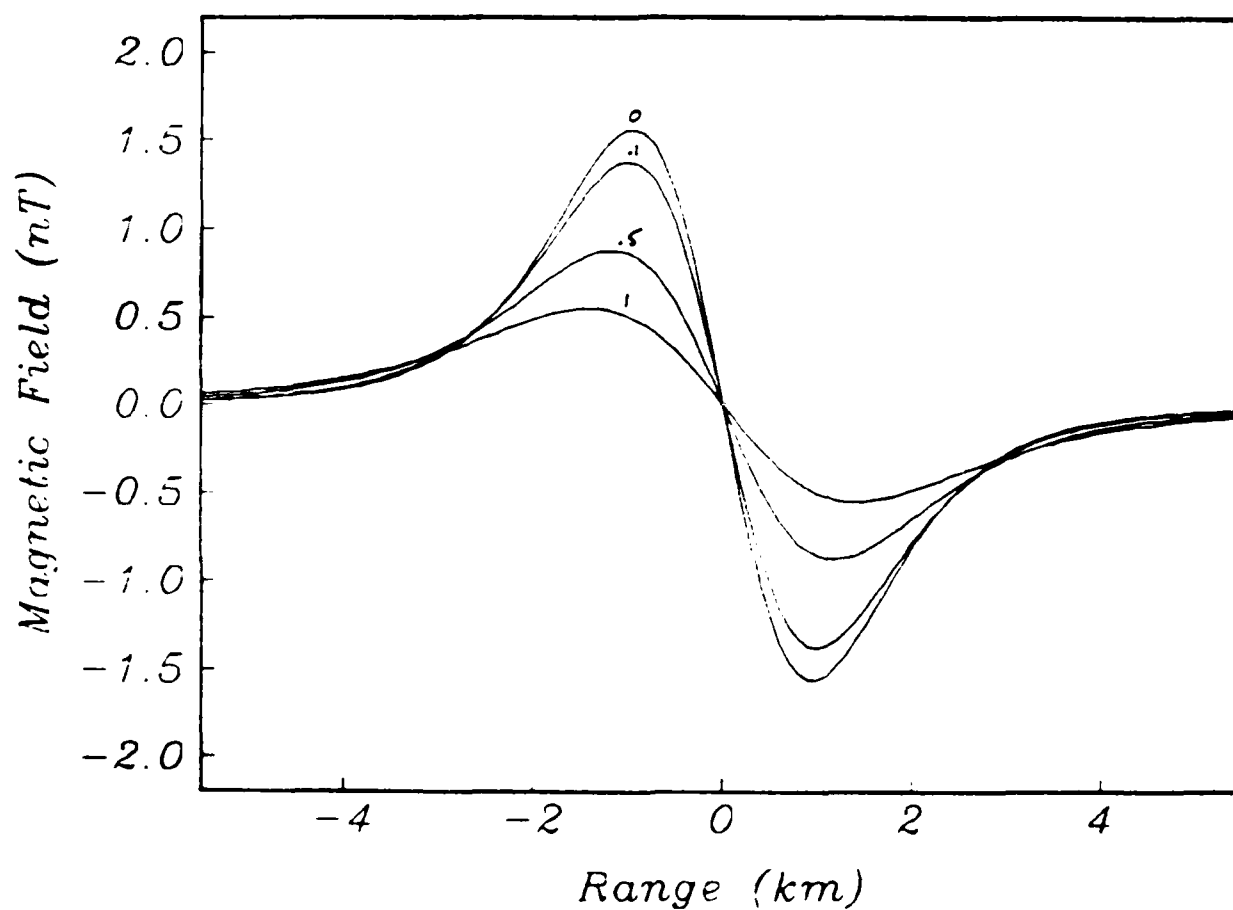


**Figure 3.** The  $B_x^z$  component of the magnetic field given by (62) for the Andaman Sea soliton parameters in Table 1, a seawater conductivity of 3.2 S/m, and a seafloor conductivity of 0.005 S m. The values at the sea-surface ( $z = 0$ ) and altitudes of 100, 500, and 1000 m are shown. See text for details

Andaman Sea  $B_z^x$  at 0, .1, .5, and 1 km

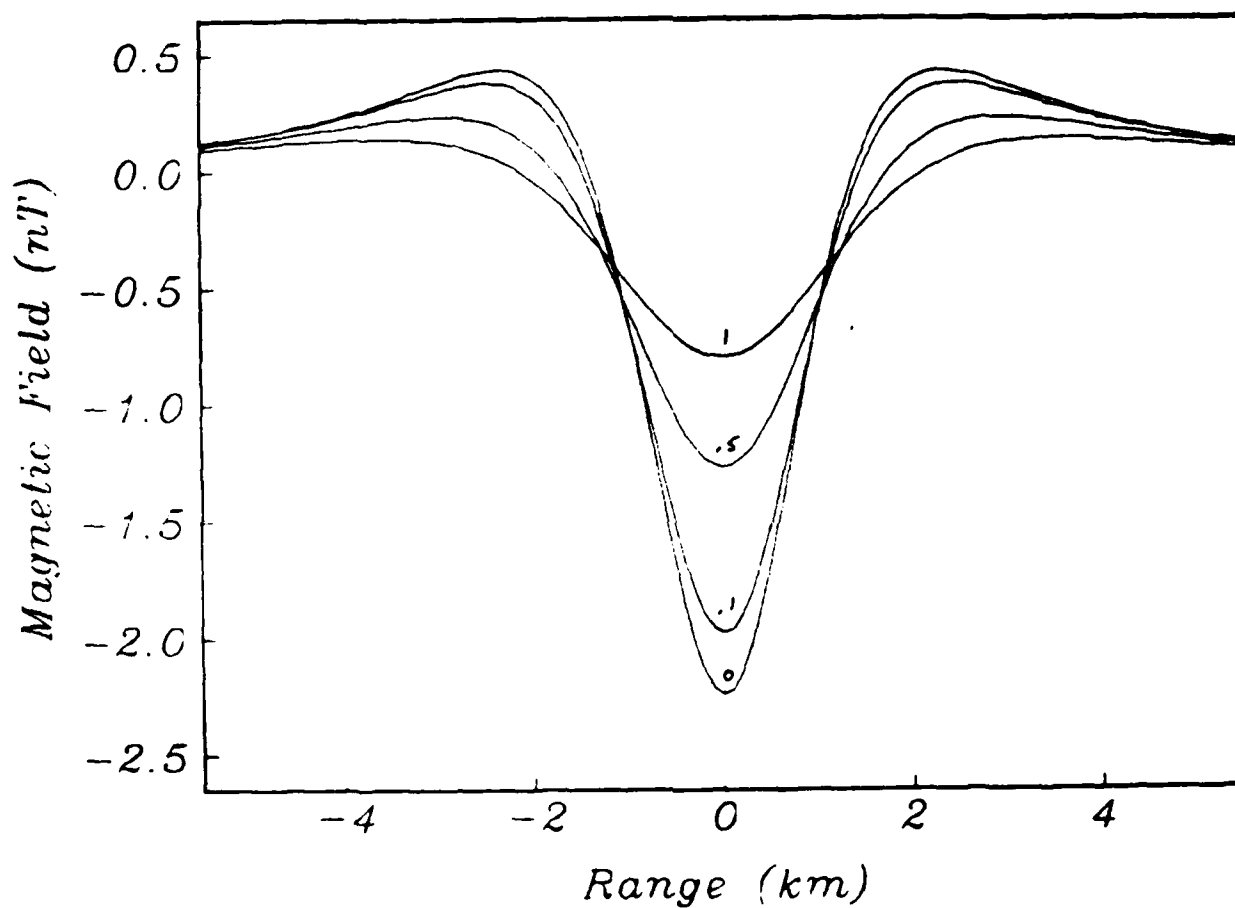


**Figure 4.** The  $B_z^x$  component of the magnetic field given by (63) for the Andaman Sea soliton parameters in Table 1, a seawater conductivity of 3.2 S/m, and a seafloor conductivity of 0.005 S/m. The values of the sea-surface ( $z = 0$ ) and altitudes of 100, 500, and 1000 m are shown. See text for details.

*Andaman Sea  $B_z^2$  at 0,.1,.5, and 1 km*

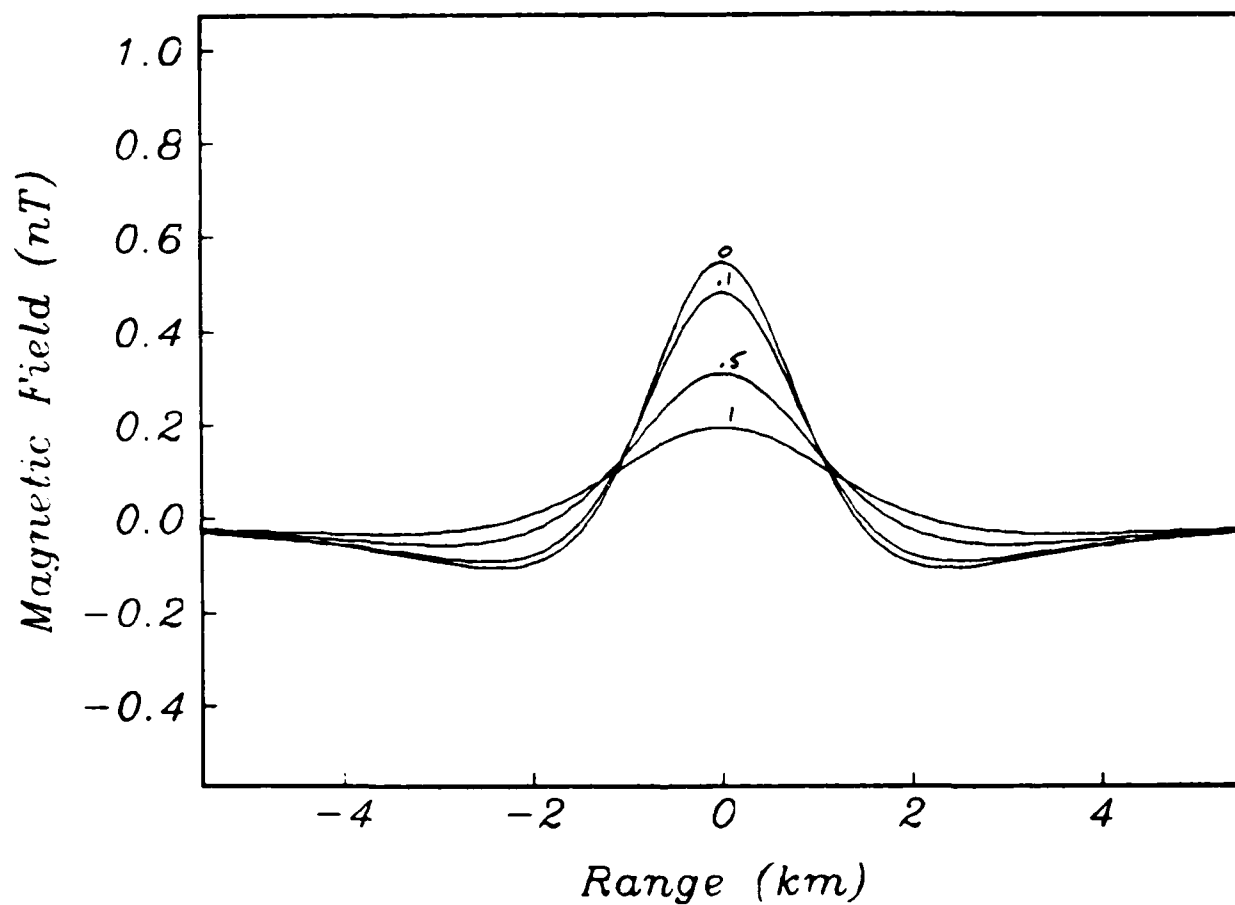


**Figure 5.** The  $B_z^2$  component of the magnetic field given by (66) for the Andaman Sea soliton parameters in Table 1, a seawater conductivity of 3.2 S/m, and a seafloor conductivity of 0.005 S/m. The values at the sea-surface ( $z = 0$ ) and altitudes of 100, 500, and 1000 m are shown. See text for details.

Andaman Sea  $B_z^z$  at 0, .1, .5, and 1 km

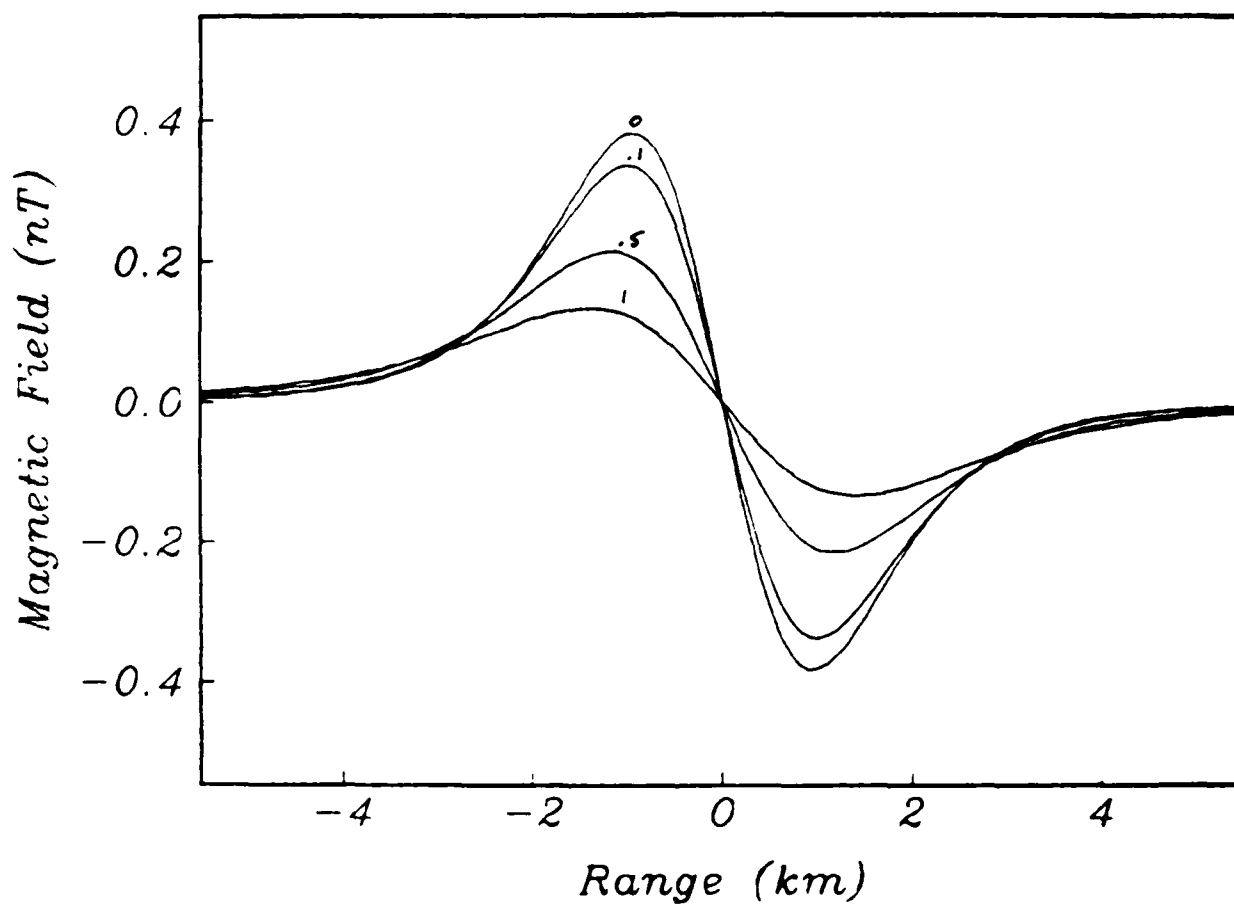


**Figure 6.** The  $B_z^z$  component of the magnetic field given by (67) for the Andaman Sea soliton parameters in Table 1, a seawater conductivity at 3.2 S/m, and a seafloor conductivity of 0.005 S/m. The values at the sea-surface ( $z = 0$ ) and altitudes of 100, 500, and 1000 m are shown. See text for details.

*Andaman Sea  $B_x$  at 0, .1, .5, and 1 km*

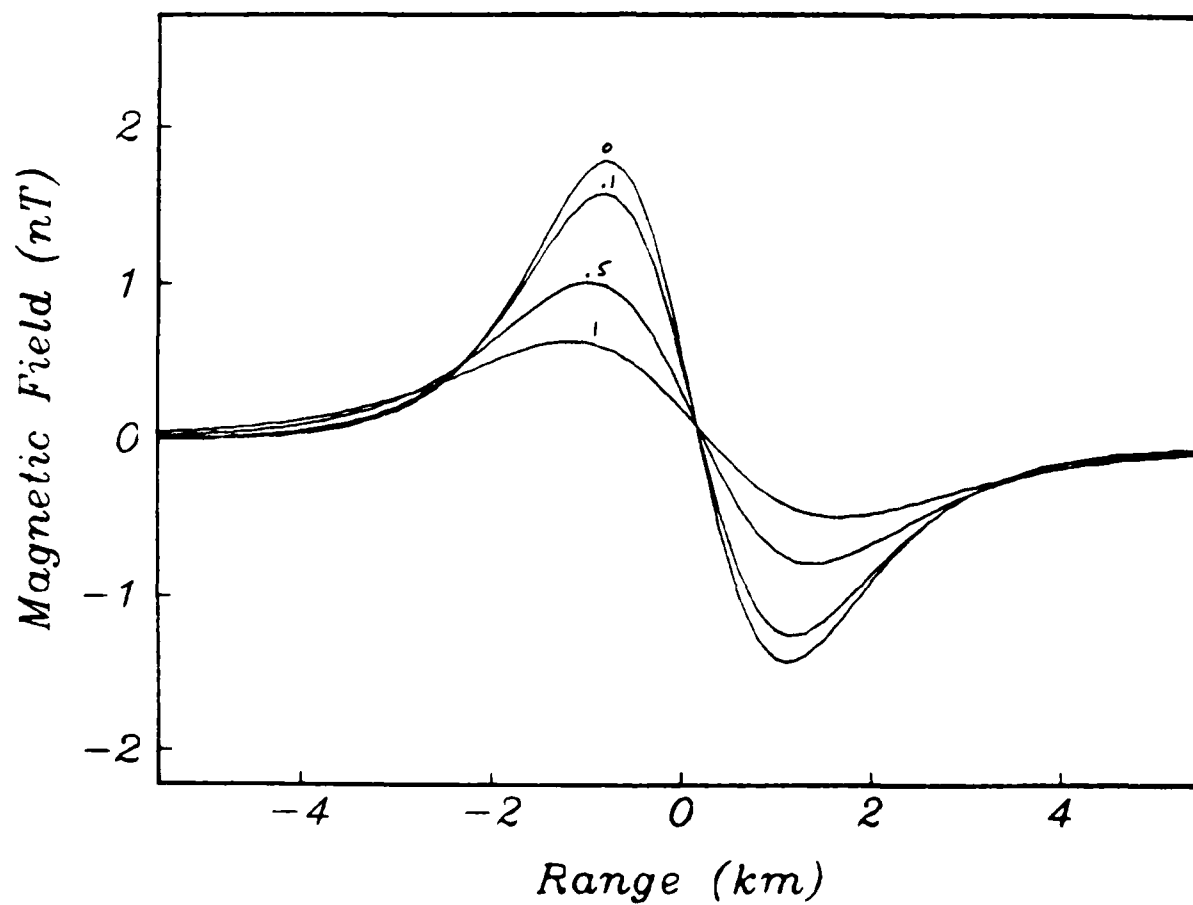


**Figure 7.** The horizontal magnetic field for the Andaman Sea soliton propagating to the north obtained by summing the results in Figures 3 and 5. A soliton moving to the east would produce the anomaly in Figure 5 alone.

*Andaman Sea  $B_z$  at 0, .1, .5, and 1 km*

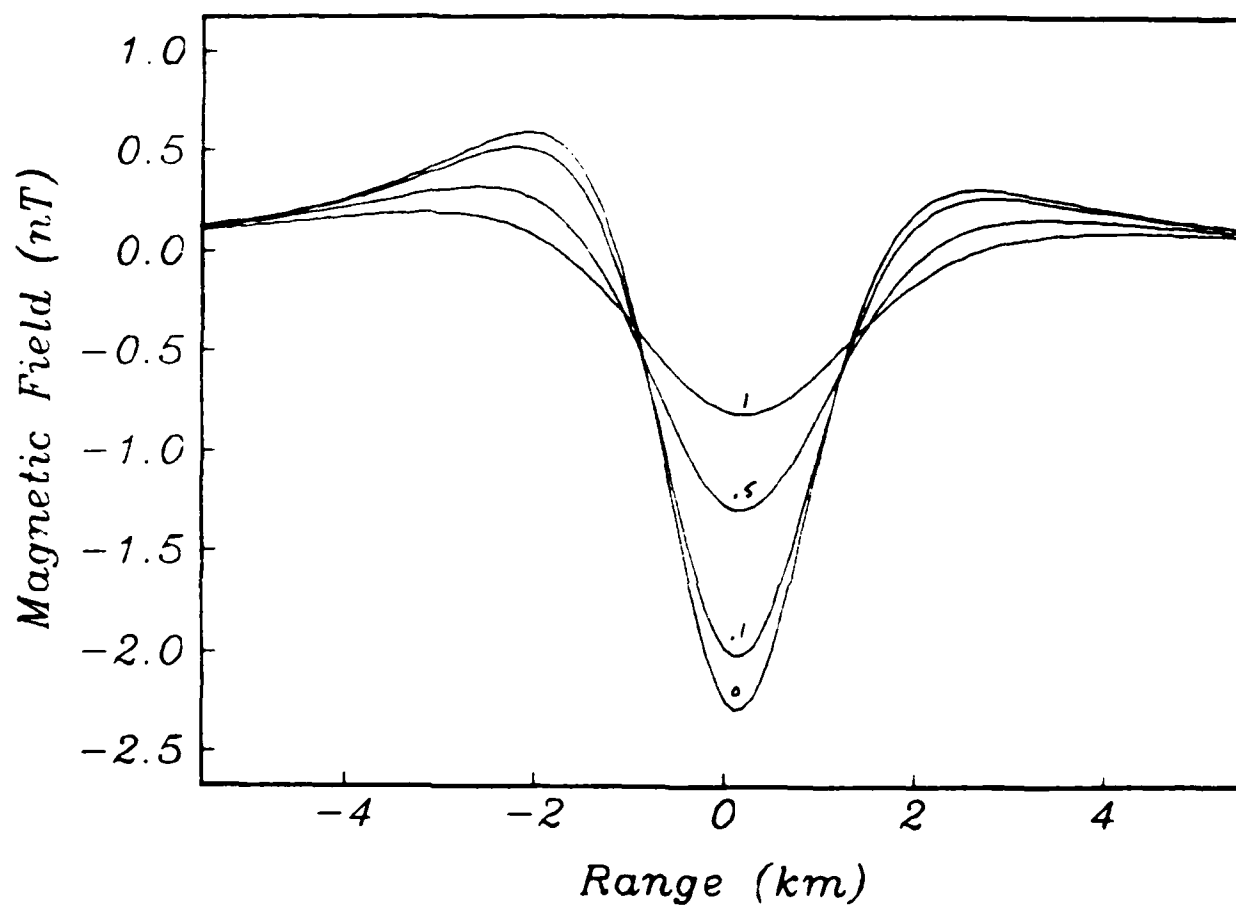


**Figure 8.** The vertical magnetic field for the Andaman Sea soliton moving to the north obtained by summing the results in Figures 4 and 6. A soliton moving to the east would produce the anomaly in Figure 6 alone.

*Andaman Sea Total B at 0,.1,.5, and 1 km*

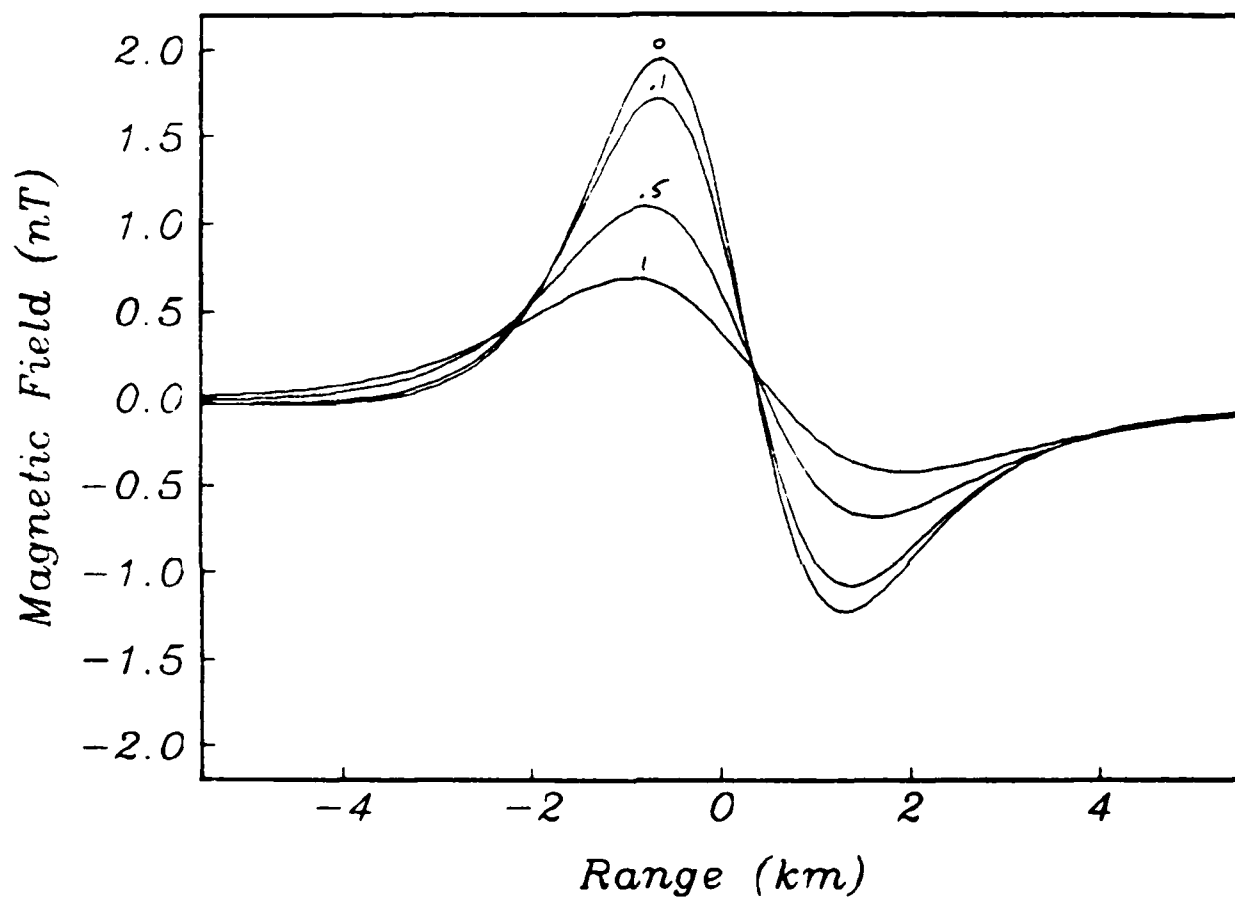


**Figure 9.** The total magnetic field anomaly for the Andaman Sea soliton propagating to the north. The size of the anomaly is controlled almost entirely by the horizontal geomagnetic field due to the low geographic latitude at this site.

*Andaman Sea Total B at 0,.1,.5, and 1 km*

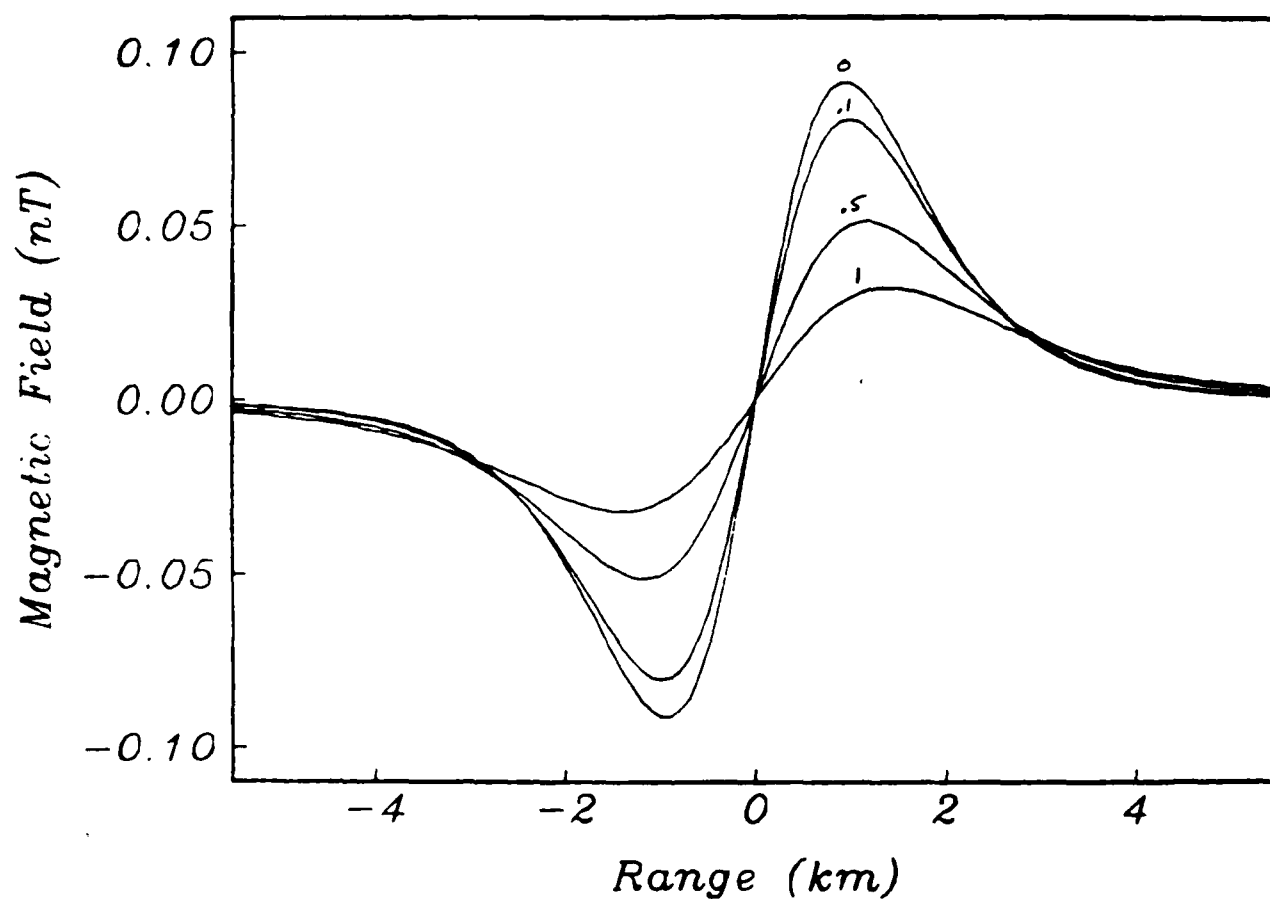


**Figure 10.** The total magnetic field anomaly for the Andaman Sea soliton propagating to the east. This anomaly is small due to its creation by interaction only with the vertical force, which is tiny at low latitudes.



*Gulf of California  $B_x$  at 0,.1,.5, and 1 km*

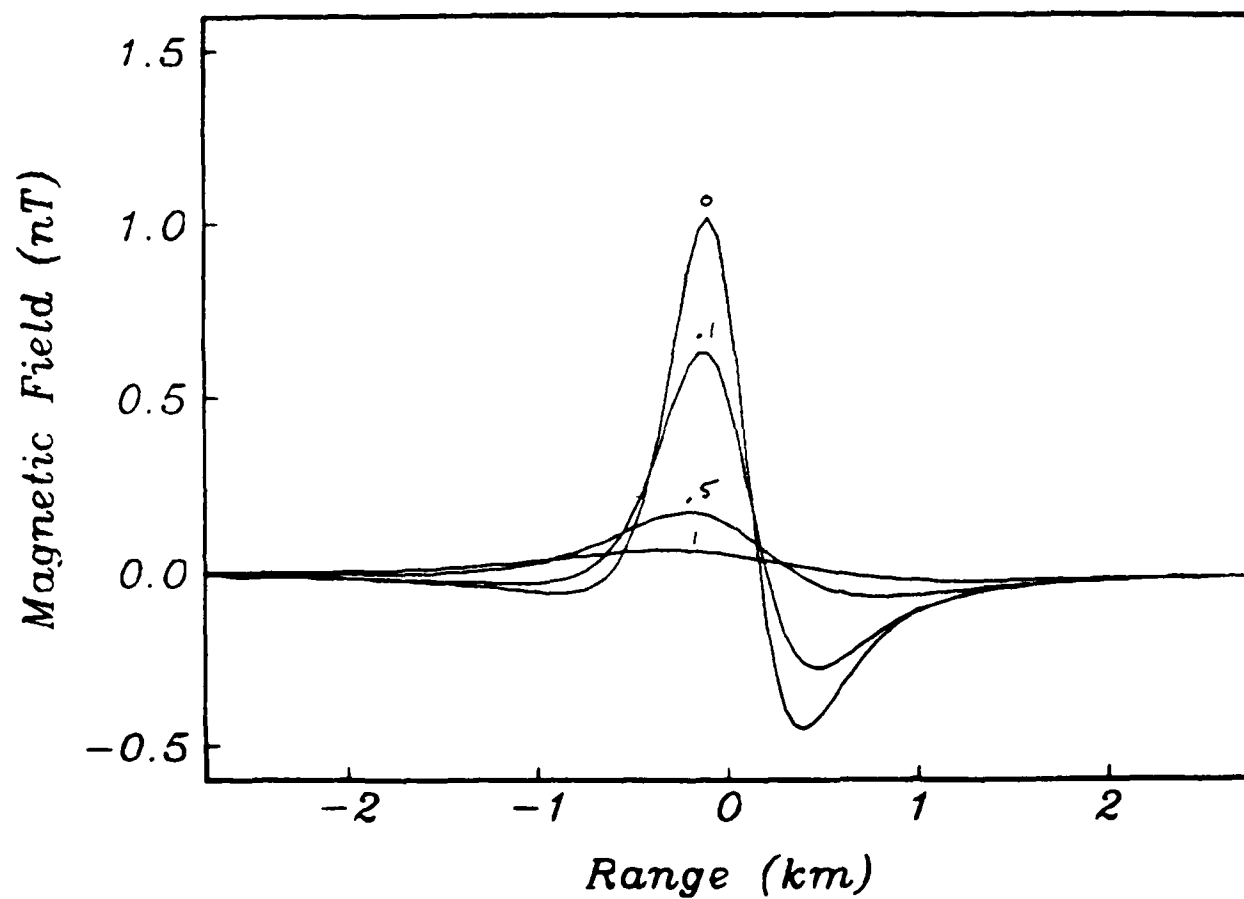


**Figure 11.** The horizontal magnetic field produced by the Gulf of California internal soliton propagating to the north.

*Gulf of California  $B_z$  at 0, .1, .5, and 1 km*

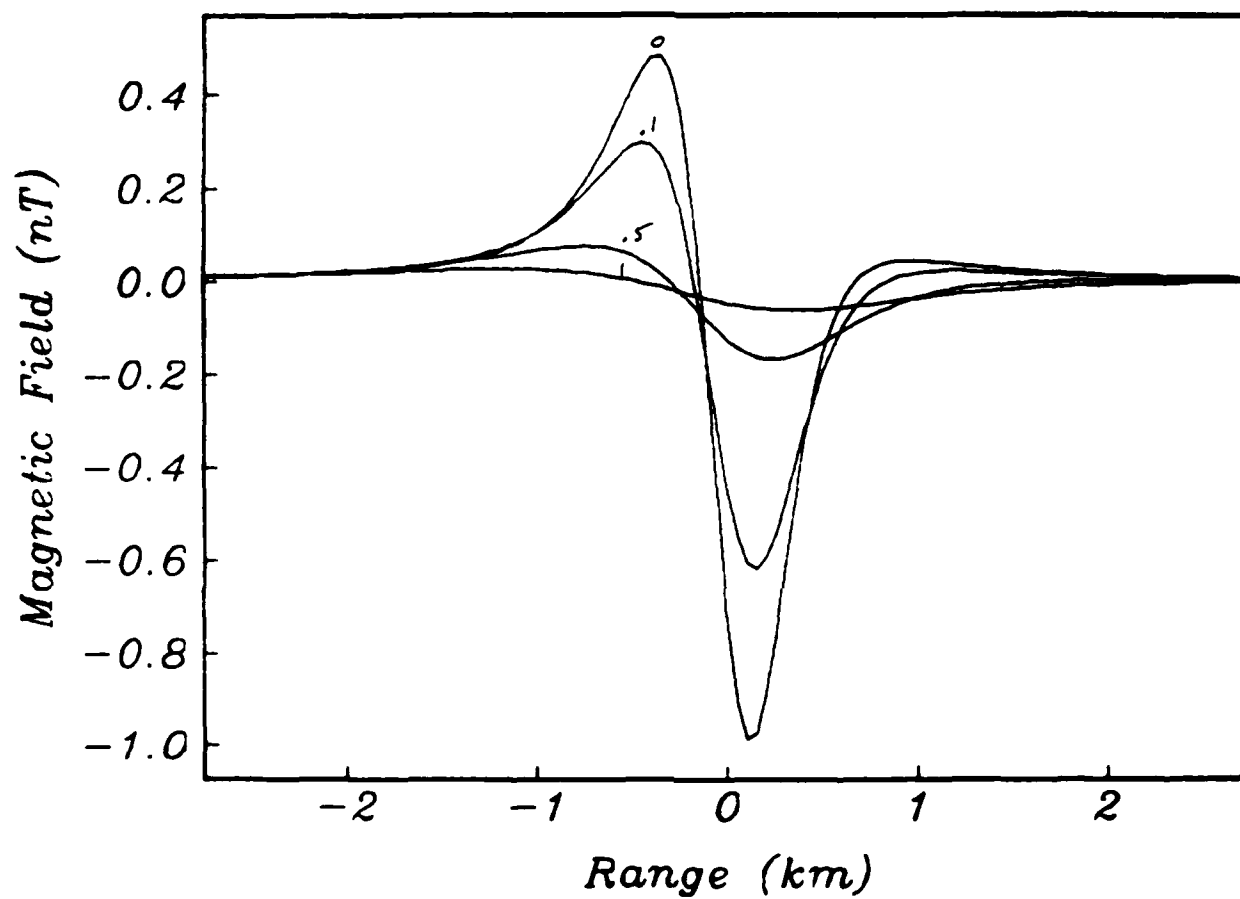


**Figure 12.** The vertical magnetic field produced by the Gulf of California internal soliton propagating to the east.

*Gulf of California Total B at 0,.1,.5, and 1 km*

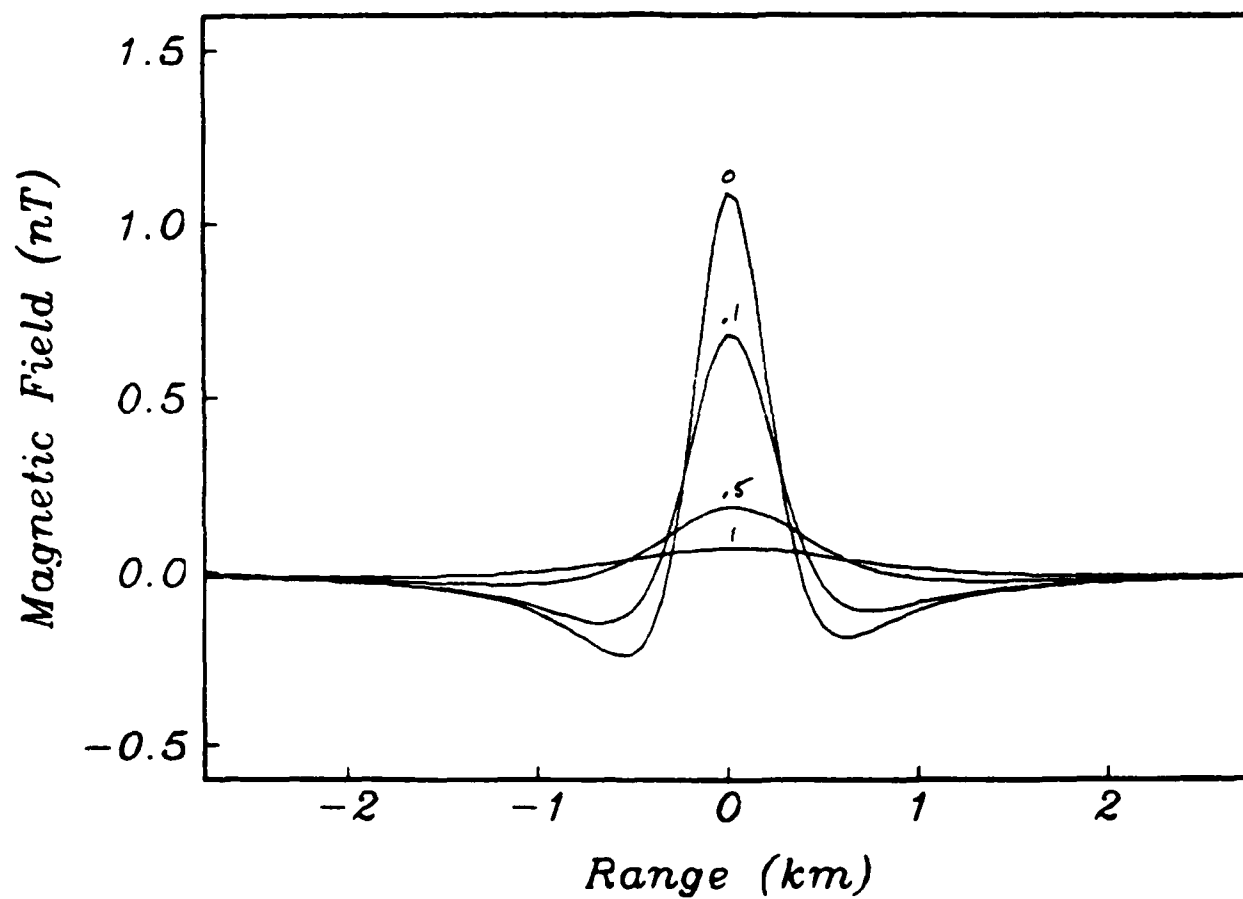


**Figure 13.** The vertical magnetic field anomaly produced by the Gulf of California internal soliton propagating to the north.

*Gulf of California Total B at 0,.1,.5, and 1 km*

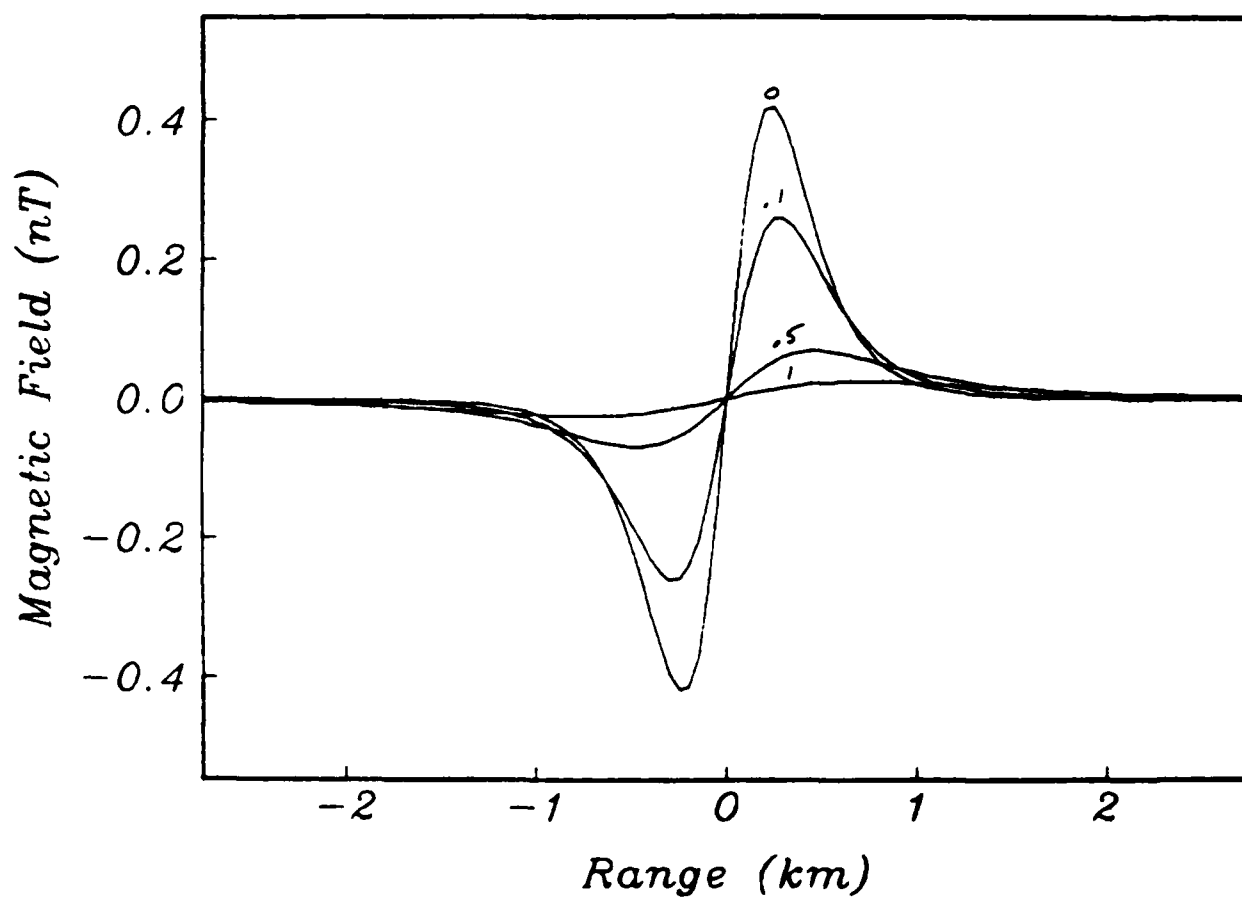


**Figure 14.** The total magnetic field anomaly produced by the Gulf of California internal soliton propagating to the east

*Massachusetts Bay  $B_x$  at 0,.05,.1, and .5 km*

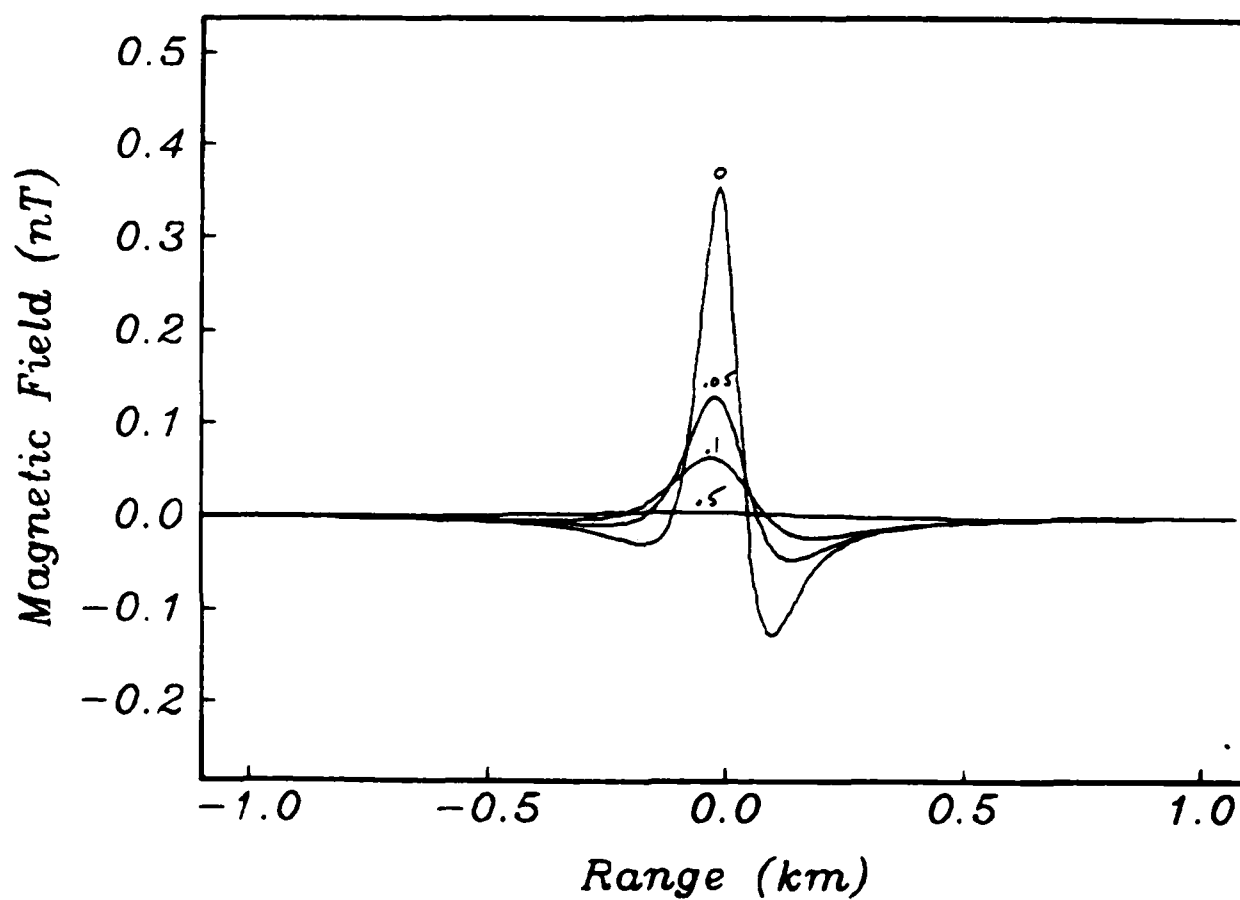


**Figure 15.** The horizontal magnetic field produced by the Massachusetts Bay internal soliton propagating to the north.

*Massachusetts Bay  $B_z$  at 0,.05,.1, and .5 km*

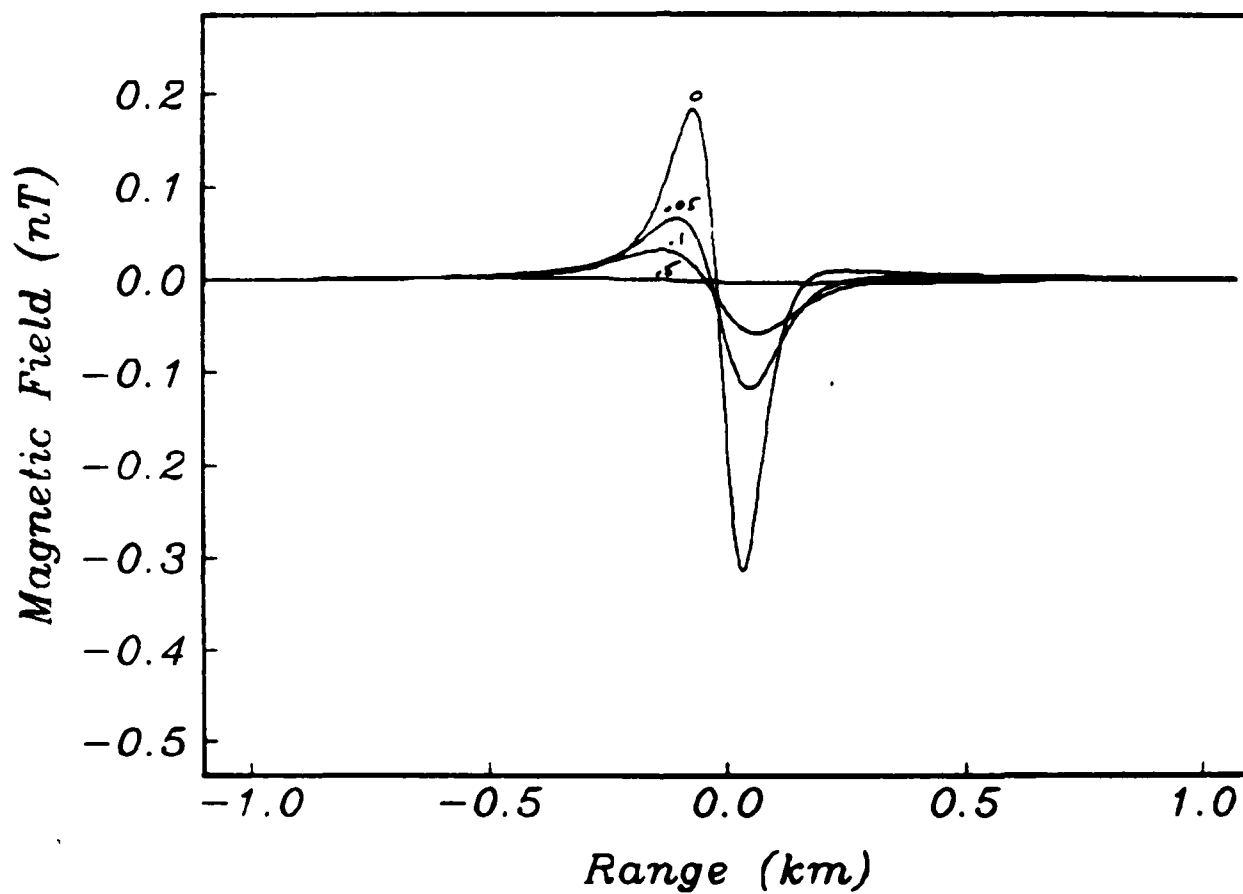


**Figure 16.** The vertical magnetic field produced by the Massachusetts Bay internal soliton propagating to the north

*Massachusetts Bay Total B at 0,.05,.1, and .5 km*

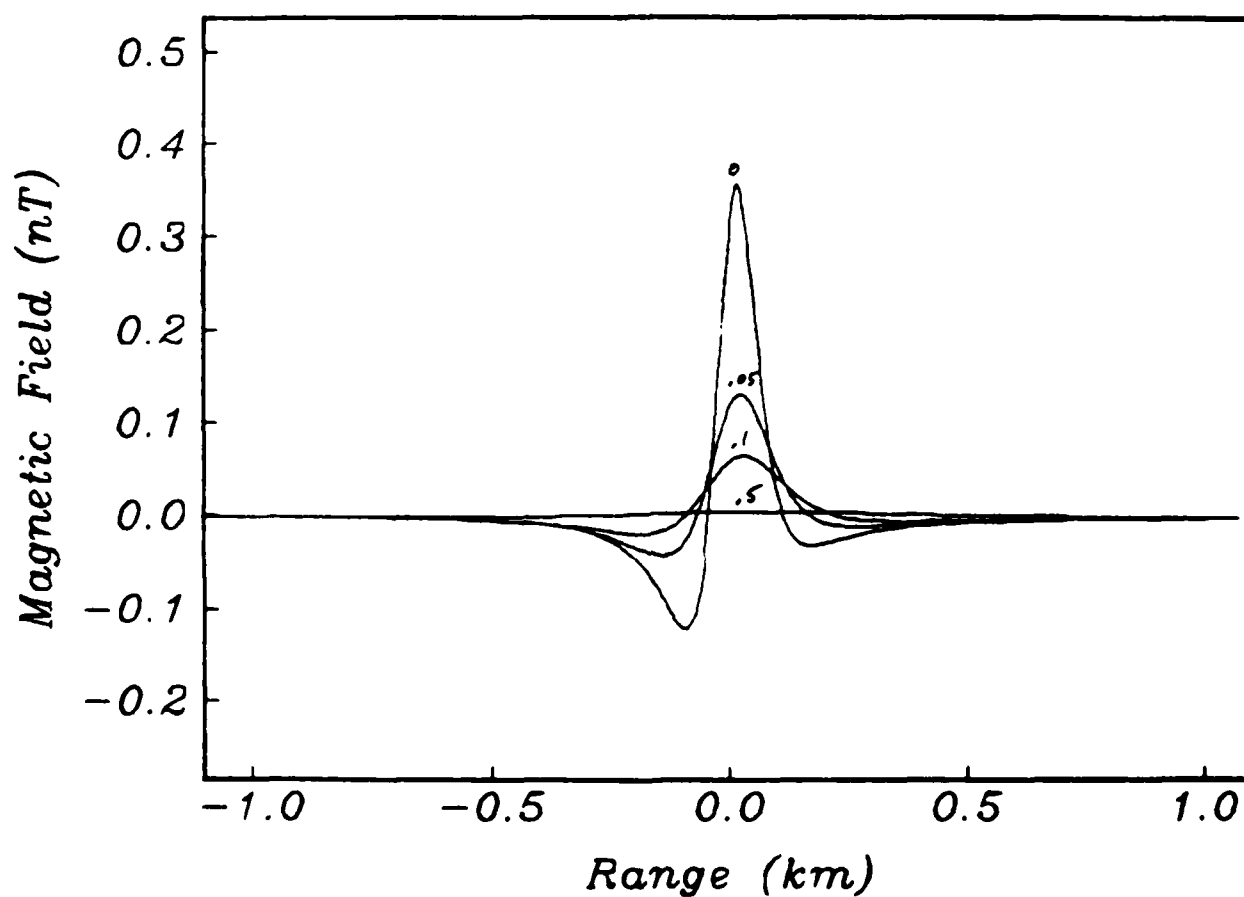


**Figure 17.** The total magnetic field anomaly for the Massachusetts Bay internal soliton propagating to the north

*Massachusetts Bay Total B at 0,.05,.1, and .5 km*

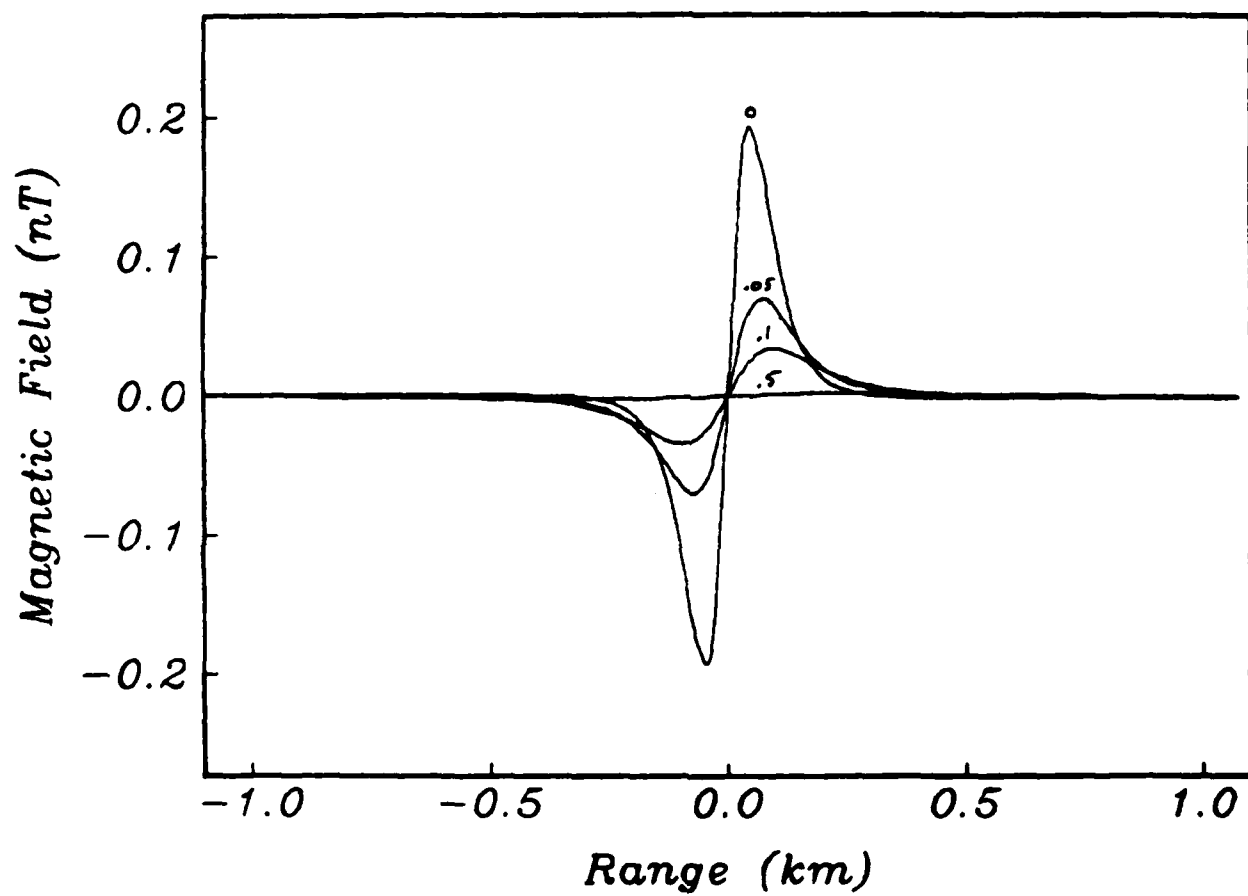


**Figure 18.** The total magnetic field anomaly for the Massachusetts Bay internal soliton propagating to the east



# Andaman Sea $B_x$ and $B_z$ at Seafloor

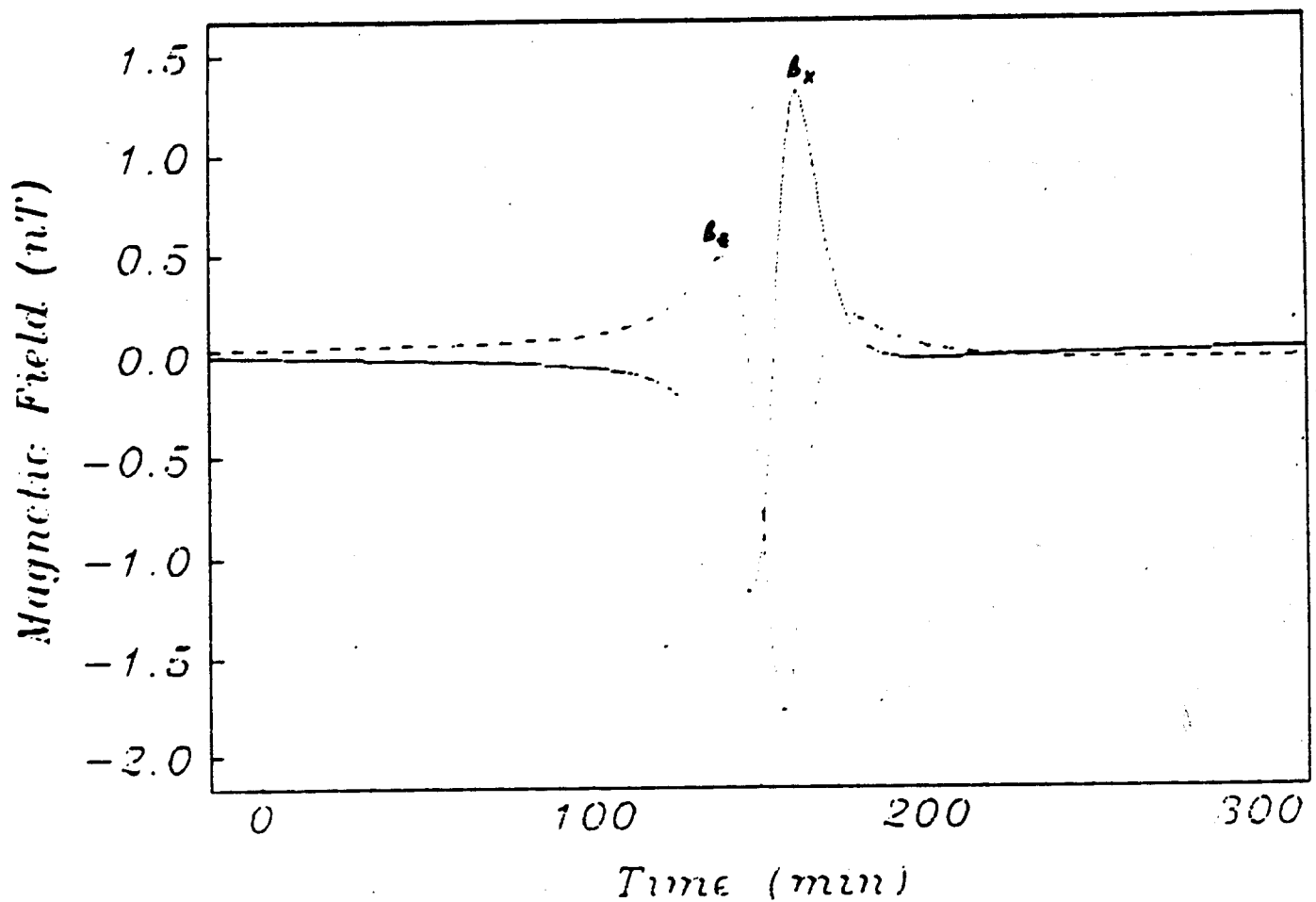


**Figure 19.** The horizontal (solid) and vertical (dashed) magnetic fields at the seafloor for the Andaman Sea internal soliton propagating to the north. The sensor position is assumed fixed, and the time-evolution of the magnetic field is shown.

*Gulf of California  $B_x$  and  $B_z$  at Seafloor*

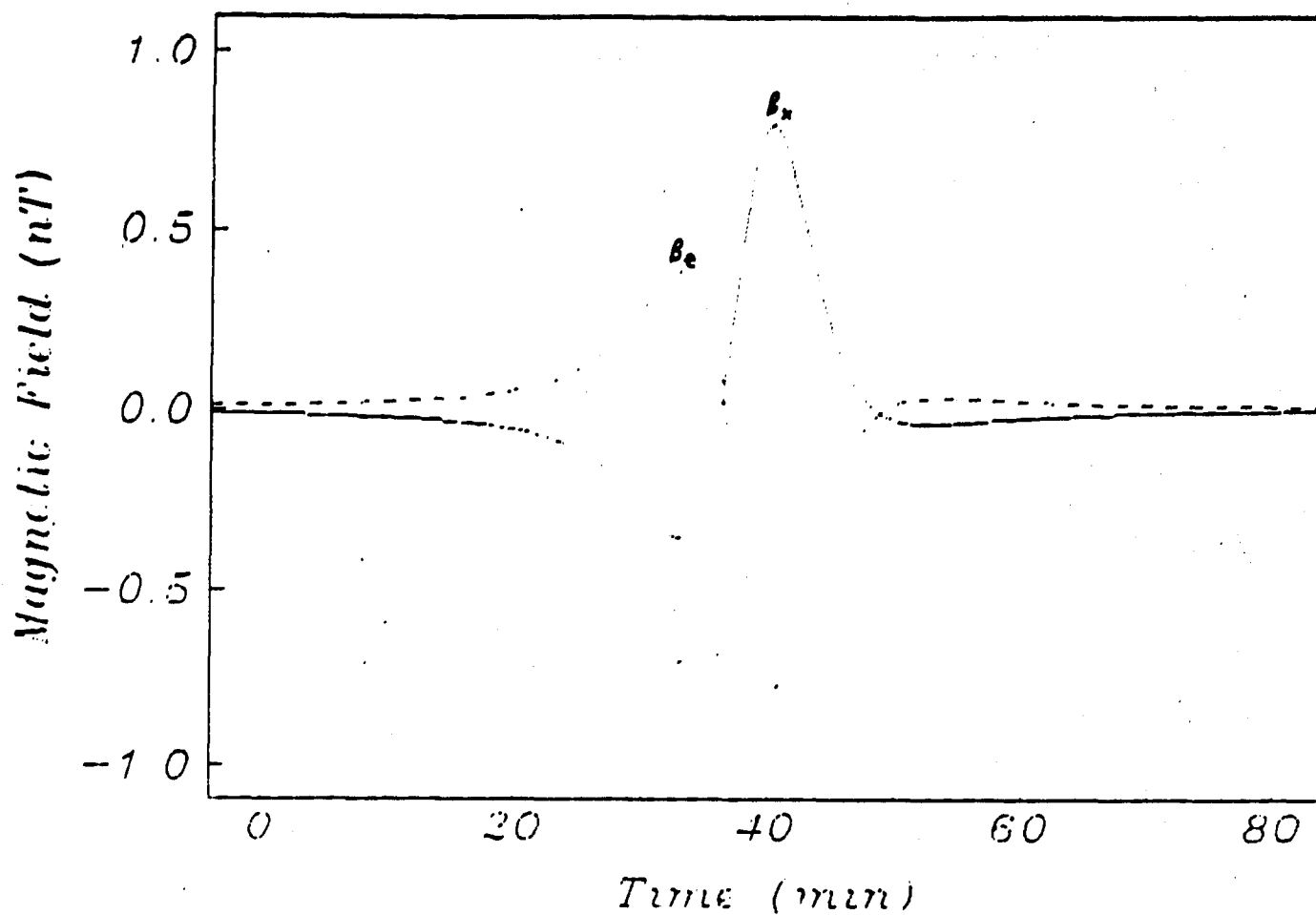


**Figure 20.** The horizontal (solid) and vertical (dashed) magnetic fields at the seafloor for the Gulf of California internal soliton with northward propagation.

*Massachusetts Bay  $B_x$  and  $B_z$  at Seafloor*

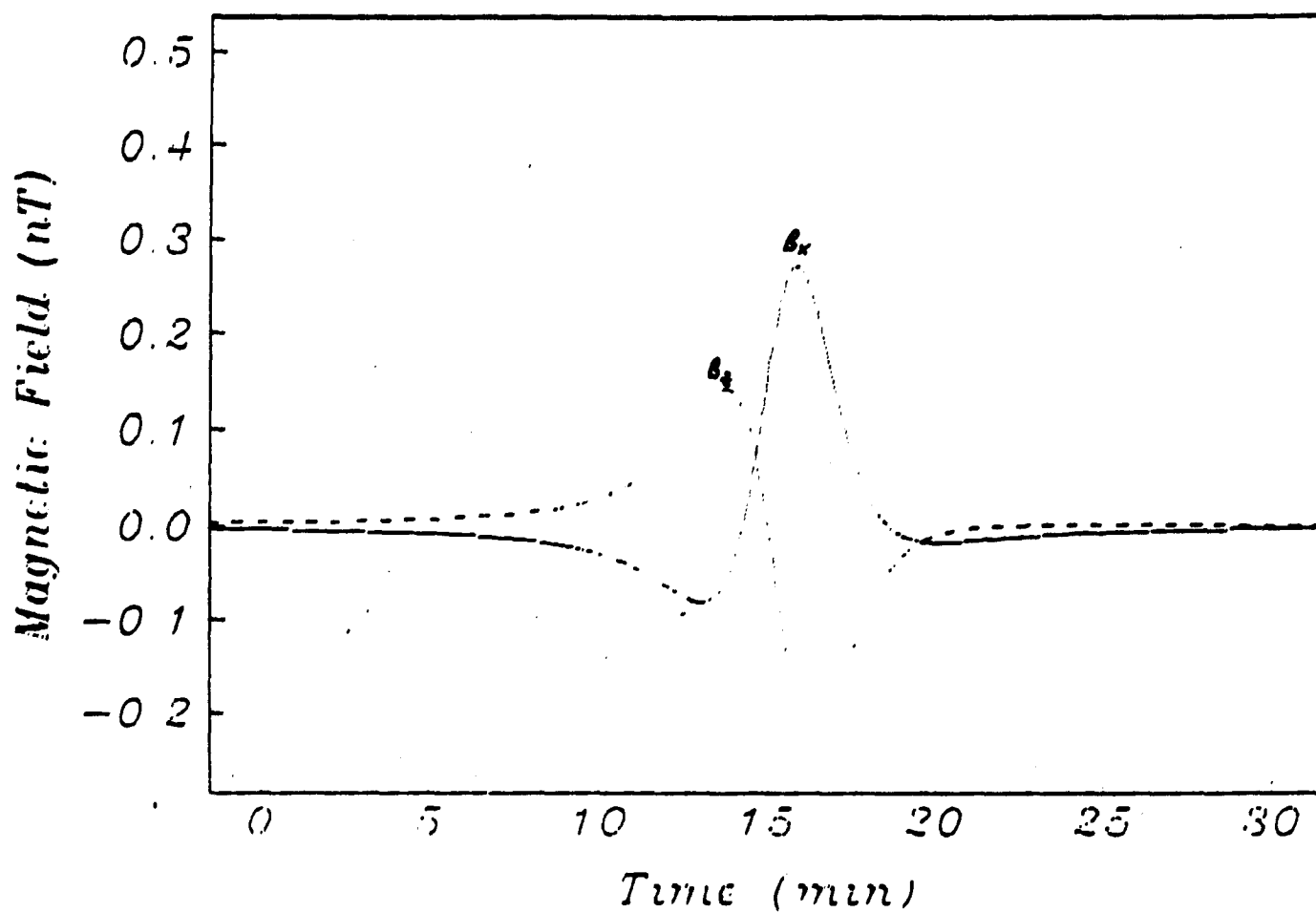


**Figure 21.** The horizontal (solid) and vertical (dashed) magnetic fields at the seafloor for the Massachusetts Bay internal soliton with eastward propagation.